



University of St Andrews

FOUNDED 1413

MRSA Populations in Nearby Care Facilities and Preferential Colonisation of Body Regions by Sequence Type

Aidan Witts

School of Medicine, University of St. Andrews



University of St Andrews

FOUNDED 1413

INTRODUCTION

Methicillin-Resistant *S. Aureus* (MRSA) infections place a significant and continuing burden on health care resources globally. They are a common type of hospital-acquired infection and the continued adaptation of the bacterium to resist antibiotic treatment is of serious concern.[1] The advent of high-throughput whole genome sequencing (WGS) technologies has enhanced our ability to monitor MRSA populations in both hospital and community settings.[2] The combination of genetic and epidemiological data provides new avenues by which we can explore patterns of colonisation and transmission.[3]

OBJECTIVES

To identify changes in the MRSA population at the monitored facilities over the three-year period for which samples were collected. To identify the impact, if any, of various sequence types on MRSA colonisation in the three body regions sampled. To compare the MRSA populations at the facilities included in the study.

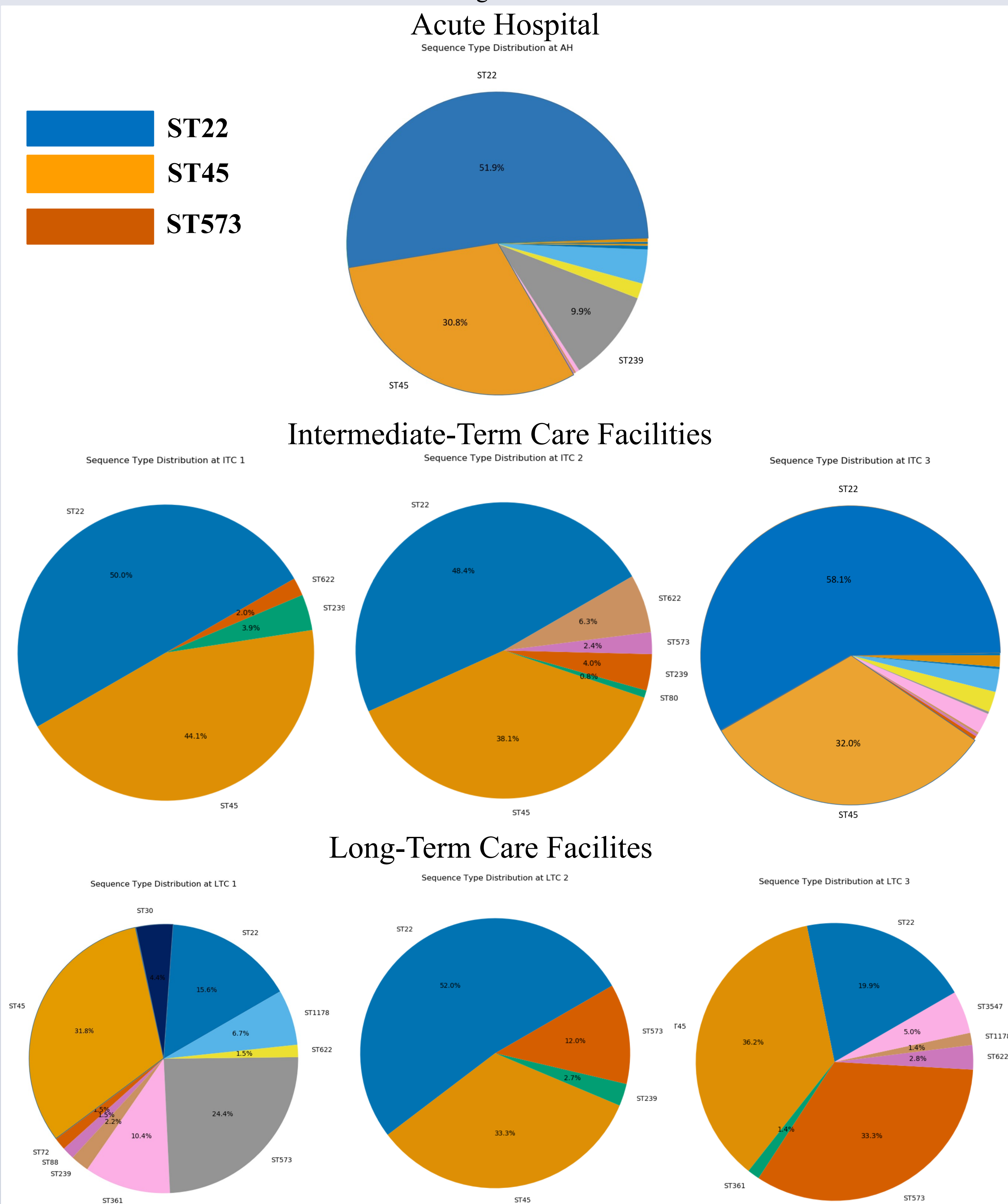
METHOD

This research used a data set generated from an acute hospital located in Singapore and six surrounding intermediate- and long-term care facilities. At each location, a population survey was performed consisting of swabs of the axilla, nares, and groin. The swabs were then cultured for the *S. aureus* bacterium, and, if positive, underwent whole genome sequencing (WGS). The WGS data was then used to determine the sequence type for each sample. These data were collected over a six-week period and the data collection was repeated over three consecutive years (2014-2016). A total of 1478 positive samples were sequenced across all locations over all three years. Exploratory and statistical analysis was performed using R and Python. Distributions of the various sequence types at each location and across time were determined to identify patterns in the population, with some further analysis focusing on the distribution of positive samples found at each of the three body regions sampled.

RESULTS

The diversity in MRSA populations at each location (displayed in Figure 1) showed significant variation. The intermediate-term care facilities tended to show the least varied populations of the location types sampled. This is especially clear for ITC 1, in which 96 of the 102 samples were ST22 or ST45 isolates. At the long-term care facilities, however, the populations were more varied. In all locations except for LTC 1, ST22 and ST45 made up the majority of the population. The acute hospital had a population most similar to those found at the intermediate-term facilities.

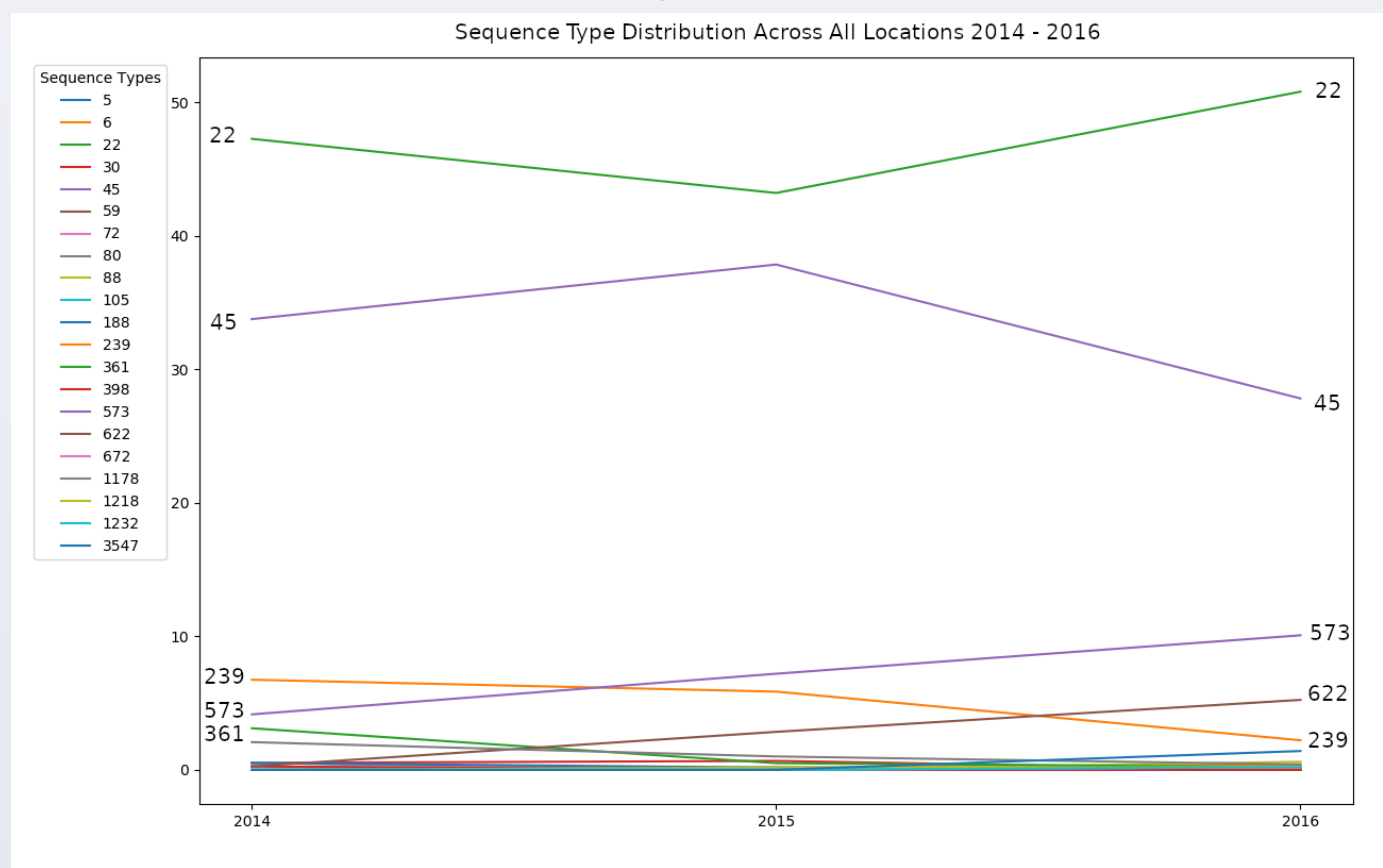
Figure 1.



RESULTS CONT.

During the three year period over which the study took place, sequence types showed only moderate population changes. The gap between ST45 and the next most prevalent ST remained in the realm of 20% throughout the study. However, there was significant change in the prevalence of some of the less dominant clones. This can be seen especially in clones such as ST239, ST573, and ST622, the populations of which changed greatly over the course of the study.

Figure 2.



The distribution of positive samples between the three areas of the body sampled was dependent on the sequence type of the MRSA bacterium. Figure 3 shows the distribution of each of the most dominant sequence types at each site. Statistical hypothesis testing was performed using the χ^2 test to determine the significance of the distribution of individual STs differing from the mean distribution across all STs. Confidence intervals were calculated using the parametric bootstrap method with a 0.95 confidence interval. The proportions in Figure 2 show substantial differences in the preferred niches of the dominant *S. aureus* clones. ST45 provides quite a striking example, with 58.8% and 31.2% of samples occupying the groin and axilla respectively.

Figure 3.

	Axilla	Groin	Nares
ST22 (n = 677) P < 0.0001	10.9% (95% CI = 8.7% - 13.3%)	43.1% (95% CI = 39.4% - 47.0%)	45.9% (95% CI = 42.1% - 49.6%)
ST45 (n = 468) P < 0.0001	10.0% (95% CI = 7.3% - 12.8%)	58.8% (95% CI = 54.3% - 63.2%)	31.2% (95% CI = 26.9% - 35.3%)
ST239 (n = 70) P = 0.0028	8.6% (95% CI = 2.9% - 15.7%)	32.9% (95% CI = 21.4% - 44.3%)	58.6% (95% CI = 47.1% - 70.0%)
ST573 (n = 109) P = 0.0002	22.9% (95% CI = 15.6% - 31.2%)	48.6% (95% CI = 39.4% - 57.8%)	28.4% (95% CI = 20.1% - 36.7%)

The P values in the above figure refer to the probability that the distribution for that ST across the three body regions is not significantly different from the mean distribution of all other STs included in the study.

CONCLUSION

MRSA populations in these health care facilities showed different degrees of variation depending on the facility from which they were sampled. The long-term care facilities stood out as maintaining a much more varied MRSA population. This may be of interest with regard to transmission patterns between the facilities.

The ST22 and ST45 clones dominated the MRSA population across all facilities. However, the prevalence of less dominant clones was considerably less static. With some clones such as ST239 almost disappearing and ST622 moving from just a few samples in 2014 to more than 5% of total samples in 2016.

Potentially the most interesting finding is that the sequence types preferentially colonise different sites on the body. Not only this, but they do so to a substantial degree with some sequence types showing nearly twice the affinity for some sites as compared to other sequence types. This raises some interesting questions regarding the adaptations that underlie these preferred niches.

REFERENCES

- [1] Monaco M, Araujo FPde, Cruciani M, Coccia EM, Pantosti A. Worldwide Epidemiology and Antibiotic Resistance of *Staphylococcus aureus* [Internet]. SpringerLink. Springer, Cham; 1970 [cited 2019Sep2]. Available from: <https://link.springer.com/chapter/10.1007/978-2-016-3>
- [2] Coleman, C. D. C. A, Goering, V. R, Stefan. Editorial: New Insights and Updates on the Molecular Epidemiology and Antimicrobial Resistance of MRSA in Humans in the Whole-Genome Sequencing Era [Internet]. Frontiers. Frontiers; 2019 [cited 2019Sep2]. Available from: <https://www.frontiersin.org/articles/10.3389/fmicb.2019.00637/full>
- [3] Jombart T, Cori A, Didelot X, Cauchemez S, Fraser C, Ferguson N. Bayesian Reconstruction of Disease Outbreaks by Combining Epidemiologic and Genomic Data [Internet]. PLOS Computational Biology. Public Library of Science; [cited 2019Sep2]. Available from: <https://journals.plos.org/ploscompbiol/article?id=10.1371/journal.pcbi.1003457>

Response of Mycobacteria to different levels of Hydrogen Peroxide and Isoniazid

Chin J. and Hammond RJH.
School of Medicine, University of St Andrews

Introduction

Mycobacterium tuberculosis (Mtb) currently stands amongst the top 10 causes of death worldwide. In the event of pulmonary Mtb, the bacteria encounters multiple stresses such as hypoxia, nutrient deprivation, and acidic environment [1]. Despite these stresses, Mtb is able to respond and adapt to its environment, resulting in its survival [2]. Previous studies have investigated the responses of mycobacteria when put under a single stress [1], and multiple stresses concurrently [3]. Most of these studies have shown that the stresses induces dormancy and phenotypic resistance in the bacteria. To combat this, research have strived to discover the changes that take place within the bacteria while being exposed to the stresses. For example, Xiao Jing and colleagues measured gene expression upon treatment of mycobacteria with hydrogen peroxide (H2O2). In this study, changes in lipid bodies will be measured upon treatment with H2O2 and isoniazid independently.

Aims

- Investigate the effect of hydrogen peroxide on the accumulation of lipid bodies in *Mycobacteria Smegmatis*, *Fortuitum* and *komossense*.
- Investigate the effect of isoniazid on the accumulation of lipid bodies in *Mycobacteria Smegmatis* and *Fortuitum*.

Materials and methods

Bacteria and culture

Isolates of *mycobacterium smegmatis*, *mycobacterium fortuitum* and *mycobacterium komossense* were incubated in sealed tubes in middlebrook 7H9 (Sigma-Aldrich) with 0.05% tween (Sigma-Aldrich). All species were incubated at 37°C except for *mycobacterium komossense*, which was incubated at 30°C. Viable cell count was determined by the Miles and Misra method.

Staining and fluorescence microscopy

Mycobacterial cells were stained with 1 mg/mL Nile red (Sigma–Aldrich) at room temperature for 20 minutes and a 10 mL aliquot was heat fixed onto a clean glass slide. Bacterial preparations were viewed by fluorescence microscopy at $\times 100$ (Leica DM5500) (excitation 480/40, 540/40. Emission 527/30, 645/75).

Flow cytometry

Cells were stained with Nile red as above and loaded into a round-bottomed 96-well plate. The plate was then loaded onto Millipore Guava easyCyte.

Thin layer chromatography (TLC)

Neutral lipids were extracted as per Bligh and Dyer method [5]. The bottom phase was dried on a hot plate, followed by suspension in 10uL of chloroform:methanol 2:1. 4uL of the mixture was spotted on aluminium oxide glass plates (Sigma-Aldrich). A solvent system of petroleum ether:diethyl ether:acetic acid 90:10:1 was used. The plate was then sprayed with primuline and visualised under UV light.

Results

Hydrogen Peroxide

Fluorescence microscopy

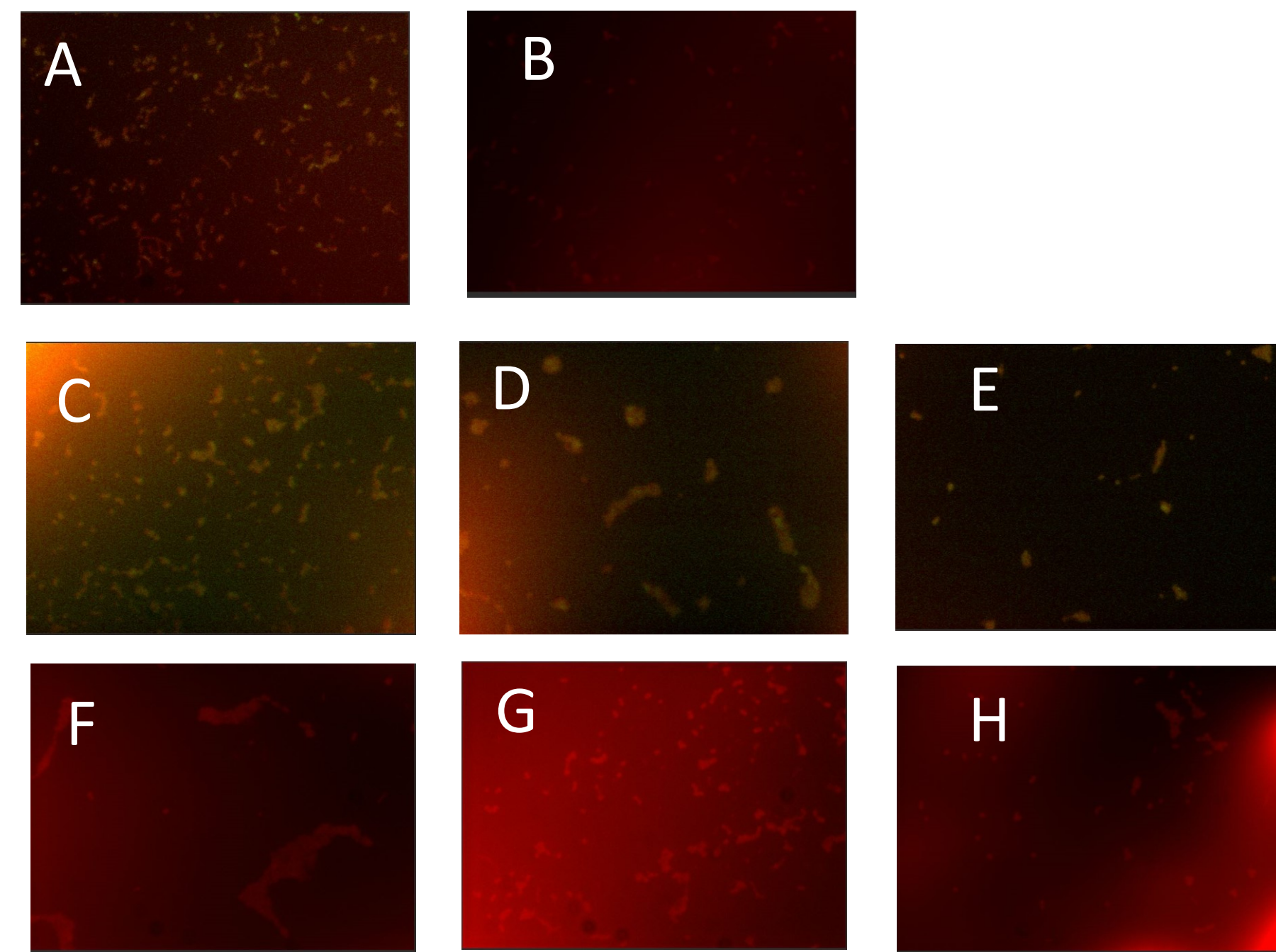


Figure 1. The effect of H2O2 on lipid body accumulation.

- A-B Similar amount of Nile Red staining, neutral lipid-containing *M. Fortuitum* population. *M. Fortuitum* cells were stained after being treated for 24 hours with H2O2 concentrations of 3mM (A) and 7mM (B). N.B. no cells could be found at 9mM.
- C-E Similar amount of Nile Red staining, neutral lipid-containing *M. Komossense* population. *M. Komossense* cells were stained after being treated for 24 hours with H2O2 concentrations of 3mM (C) and 7mM (D) and 9mM (E).
- F-H Similar amount of Nile Red staining, neutral lipid-containing *M. Smegmatis* population. *M. Smegmatis* cells were stained after being treated for 24 hours with H2O2 concentrations of 3mM (F) and 7mM (G) and 9mM (H).

Flow Cytometry

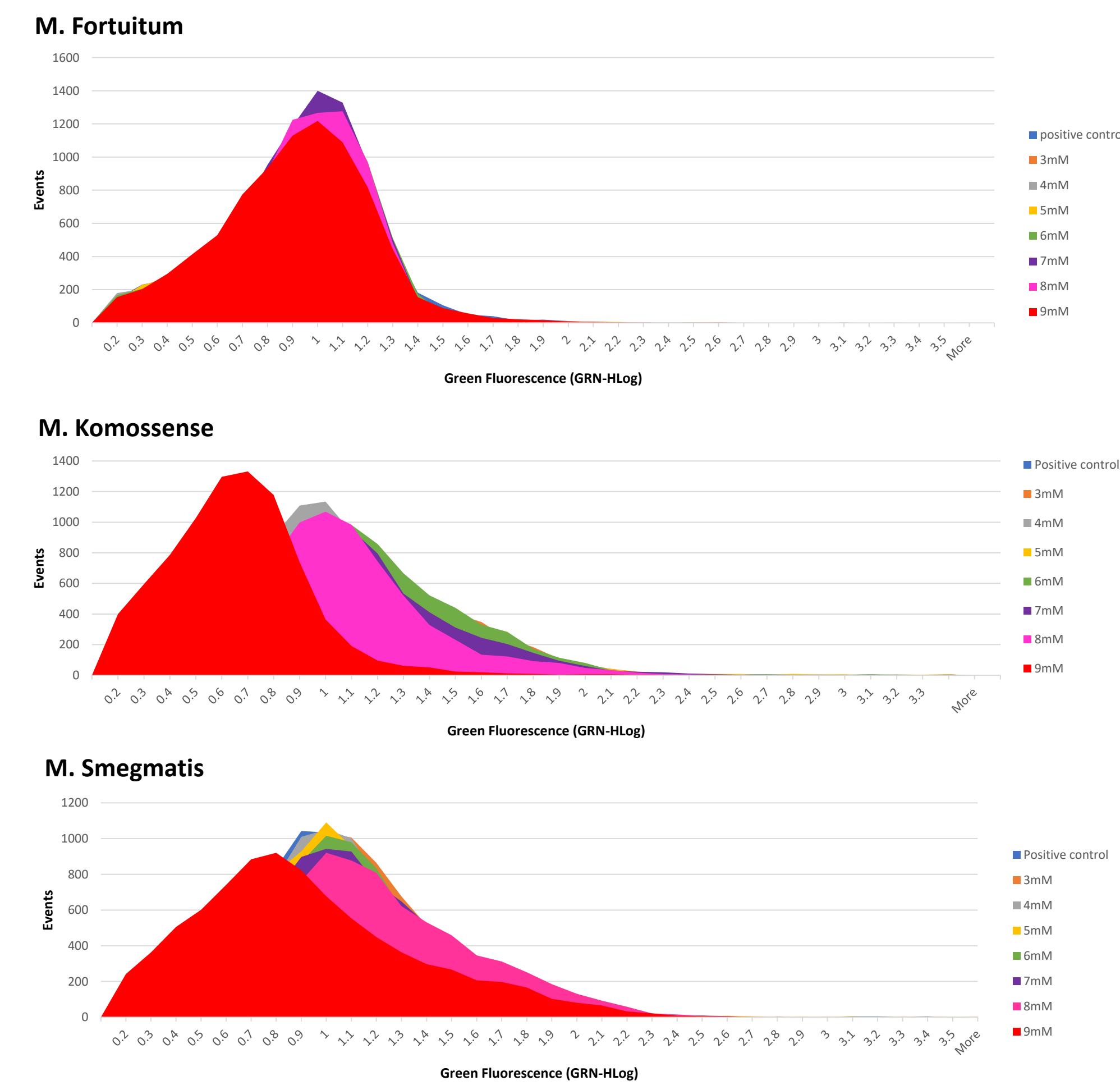


Figure 2. Comparison of M. Smeg green fluorescence at different levels of isoniazid. N.B. events in MIC x2 cannot be seen because it is identical to MIC x4. Events between 0.0 to 0.1 was omitted for simplicity reasons.

Table 1. TLC separation of neutral mycobacteria lipids after H2O2 treatment. The Rf values were as follows: cholesterol esters (CE) (0.9), triacylglycerols (TAG) (0.35), free fatty acids (FFA) (0.1), cholesterol (0.1), 1,3-diacylglycerols (0.08), 1,2 diacylglycerols (0.08) and monoacylglycerols (0.00).

	Positive control	3mM	4mM	5mM	6mM	7mM	8mM	9mM
<i>M. Fortuitum</i>	TAG	TAG	n/a	n/a	n/a	TAG	TAG	TAG
<i>M. Komossense</i>	TAG	TAG	n/a	n/a	n/a	n/a	TAG	TAG
<i>M. Smegmatis</i>	TAG	TAG	TAG	TAG	TAG	TAG	TAG	TAG

Isoniazid

Fluorescence microscopy

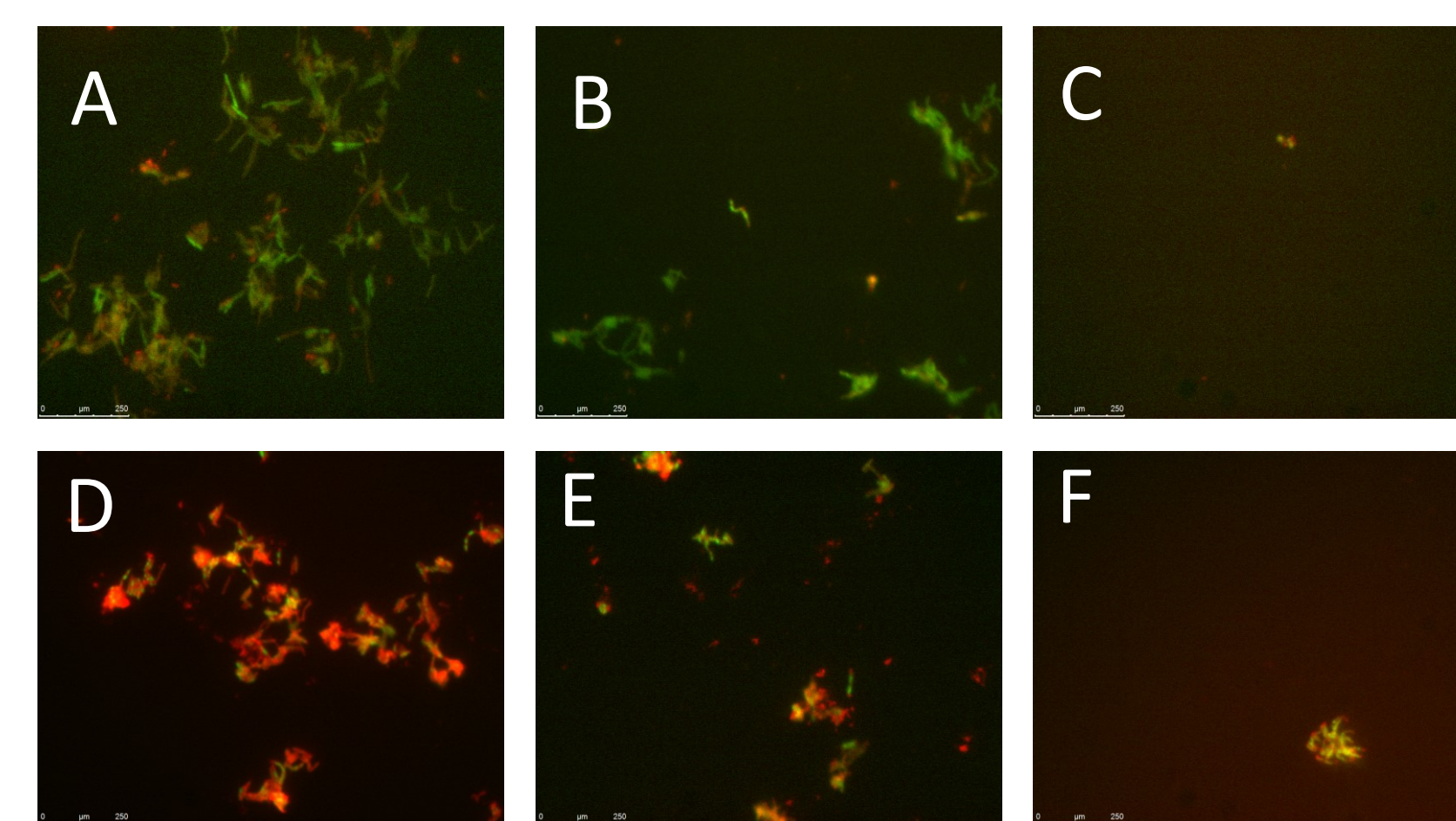


Figure 3 The effect of isoniazid on lipid body accumulation. A-C decrease in Nile Red staining, neutral lipid-containing *M. Fort* population. *M. Fort* cells were stained after being treated for 96 hours with MIC (=12.5µg/ml) x0.5 (A), MIC x1 (B) and MIC x8 (C). D-F decrease in Nile Red staining, neutral lipid-containing *M. Smeg* population. *M. Smeg* cells were stained after being treated for 96 hours with MIC (=25µg/ml) x0.5 (D), MIC x1 (E) and MIC x8 (F).

Viable cell count

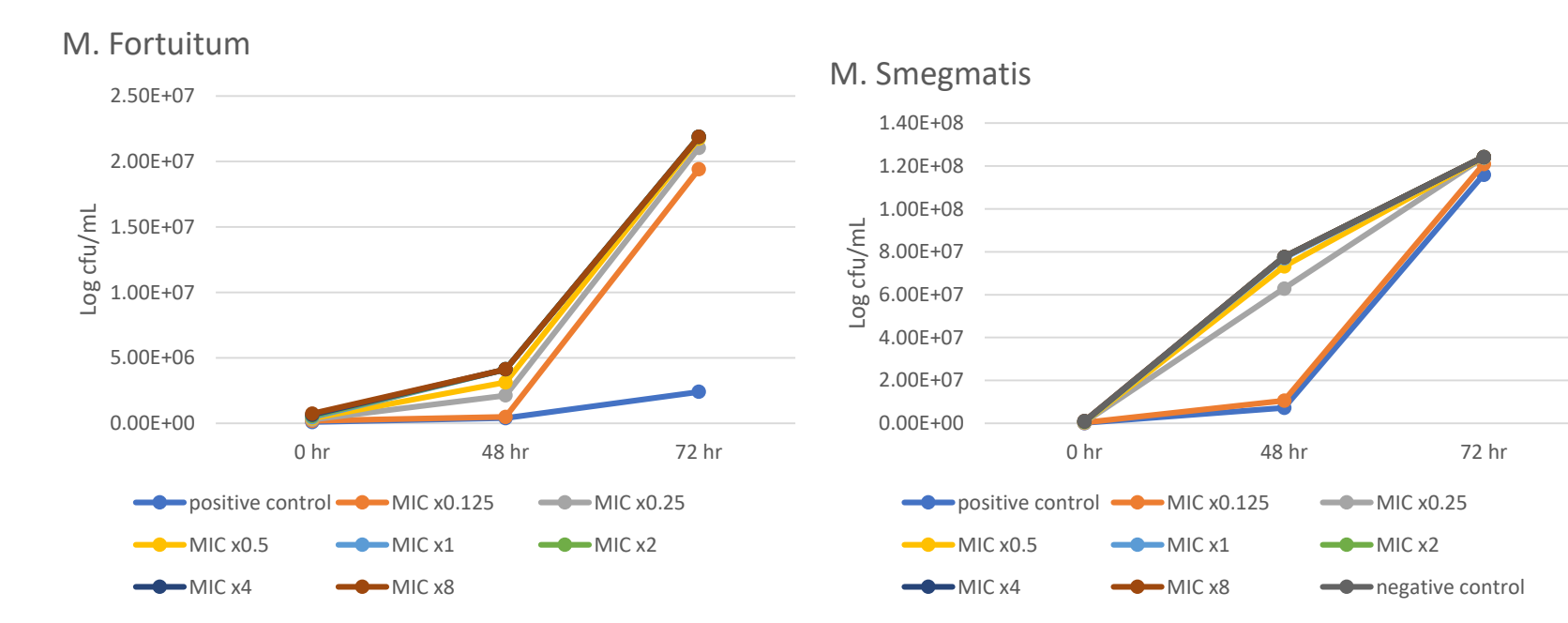


Figure 4. Viable cell count via the Miles and Mesra method. N.B. there was growth in the *M. Smeg* agar plate after 72 hrs.

Flow Cytometry

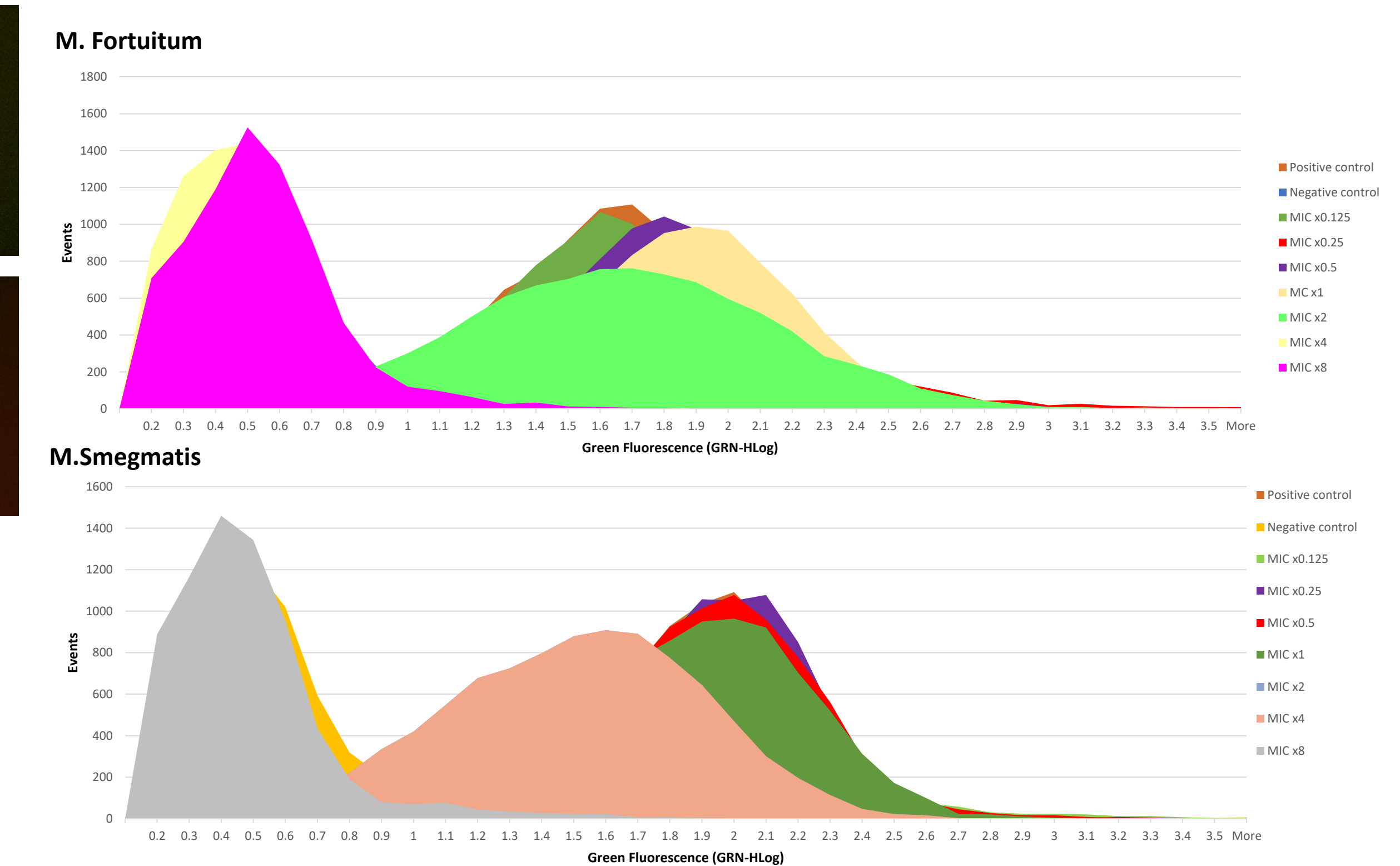


Figure 5. Comparison of M. Fort and M. Smeg green fluorescence at different levels of isoniazid. An increase in green fluorescence could be seen for *M. Fortuitum*, but not for *M. Smegmatis*. N.B. Events between 0.0 to 0.1 was omitted for simplicity reasons.

Thin Layer Chromatography

	Positive control	Negative control	MIC x0.125	MIC x0.25	MIC x0.5	MIC x1	MIC x2	MIC x4	MIC x8
<i>M. Fortuitum</i>	TAG, FFA, CE	FFA, CE	TAG, FFA, CE	TAG, FFA, CE	TAG, FFA, CE	TAG, FFA, CE	TAG, CE	TAG, CE	TAG, CE
<i>M. Smegmatis</i>	n/a	FFA	TAG, FFA	n/a	TAG, CE	TAG, CE	TAG, CE	TAG, CE	TAG, CE

Table 2. TLC separation of neutral mycobacteria lipids after isoniazid treatment. The Rf values were as follows: cholesterol esters (CE) (0.9), triacylglycerols (TAG) (0.35), free fatty acids (FFA) (0.1), cholesterol (0.1), 1,3-diacylglycerols (0.08), 1,2 diacylglycerols (0.08) and monoacylglycerols (0.00).

Discussion and Conclusion

This study has shown that when treated with hydrogen peroxide, *M. Fortuitum*, *M. Smegmatis* and *M. Komossense* do not significantly increase lipid body accumulation. Possible explanations include the cells dying too rapidly, or insufficient time for the cells to generate the lipid bodies. Perhaps 48 or 72 hours would be a more adequate time instead of 24 hours. The TLC has revealed that triacylglycerols (TAG) is the main lipid constituent in the cells' lipidome. The other half of the study looked at stressing mycobacteria with isoniazid. Here, *M. Fortuitum* generated many lipid bodies, as seen on the microscope (fig 3) and indicated by the shift in green fluorescence towards the right (fig 5). same pattern is seen in *M. Smegmatis*. Interestingly, the lipid content contained cholesterol esters as well, which wasn't found when the cells were stressed with hydrogen peroxide. In conclusion, when stressed with hydrogen peroxide, the species of mycobacteria tested didn't respond by accumulating lipid bodies; but when stressed with isoniazid, lipid bodies were generated.

References

- Batyrshina Y, Schwartz Y. Modeling of *Mycobacterium tuberculosis* dormancy in bacterial cultures. *Tuberculosis*. 2019;117:7-17.
- Zahrt TC, Deretic V. Reactive nitrogen and oxygen intermediates and bacterial defenses: unusual adaptations in *Mycobacterium tuberculosis*. *Antioxidants & redox signaling*. 2002;4(1):141–59. doi:10.1089/152308602753625924
- Deb C, Lee C, Dube Y, Daniel J, Abomoelak B, Sirakova T et al. A Novel In Vitro Multiple-Stress Dormancy Model for *Mycobacterium tuberculosis* Generates a Lipid-Loaded, Drug-Tolerant, Dormant Pathogen. *PLoS ONE*. 2009;4(6):e6077.
- Li X, Wu J, Han J, Hu Y, Mi K. Distinct Responses of *Mycobacterium smegmatis* to Exposure to Low and High Levels of Hydrogen Peroxide. *PLoS ONE*. 2015;10(7):e0134595.
- Bligh, E.G. and Dyer, W.J. 1959. A rapid method for total lipid extraction and purification. *Can. J. Biochem. Physiol.* 37:911-917.



Sex difference in spatial memory: A fact or a myth? A T₂ relaxometry and stereologic volumetry study

Luciana CROWTHER, Enis CEZAYIRLI

INTRODUCTION

Memory as defined by the Oxford English Dictionary is “the faculty by which the mind stores and remembers information”¹. The concept of memory is crucial in our everyday lives, it allows us to learn, understand and communicate knowledge which has been processed by a complex collection of structures believed to reside within the brain. This ability to decipher and manipulate information that we are constantly exposed to alongside recalling past experiences has the power to dictate our behaviour and the decisions we make in order to function. Kessels et al.² states that “spatial memory involves the ability to encode, store and retrieve information” which encompasses route navigation and object location. Our study looked at this aspect of memory and investigated whether there are differences between men and women through quantitative evaluation of certain brain regions.

Our understanding of memory and the cognitive functions of the brain has vastly evolved since the 1880s when proposed theories and what we recognise as modern memory investigations were first recorded (Hermann Ebbinghaus, 1885)³. Research into understanding cognitive functions can be grouped into three main categories; case studies, animal models and more recently functional imaging. Human studies demonstrate the challenges of understanding the function in the living. The outcome of the surgery of Patient HM (Figures 1 and 2), an epileptic patient who suffered from intractable seizures was the major breakthrough. Following the bilateral removal of his medial temporal lobes in hope of treatment, HM was left with mild retrograde and severe anterograde amnesia⁴. This publication triggered research on all aspects of memory.



Figure 1: Patient HM in 1953 before his surgery

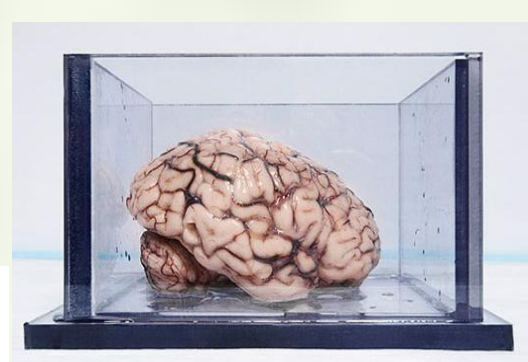
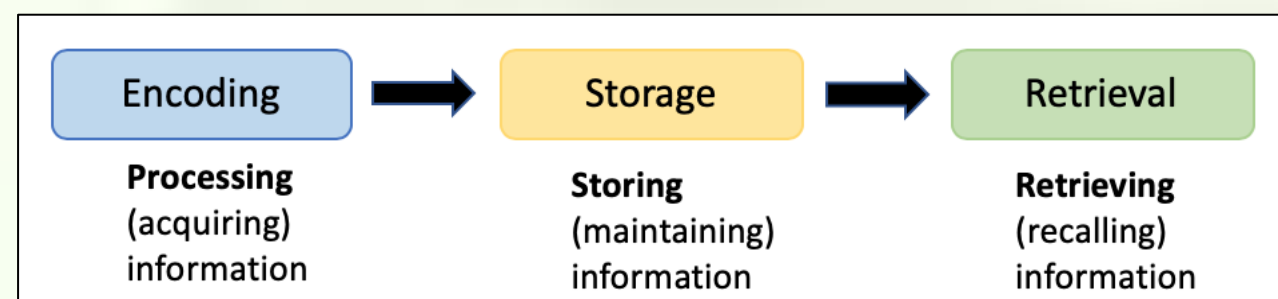


Figure 2: Patient HM's brain, before it was sectioned

We have learned a great deal about the neural basis of memory by observing outcomes of cases in history where the integrity of normal brain structure was compromised, which resulted in memory impairment.

The next step in investigating memory was the development of animal models, pioneered by Mortimer Mishkin⁵ and Stuart Zola-Morgan and coworkers⁶, since memory is exhibited across the animal kingdom. Animal models made it possible to investigate systematically which anatomical structures are involved in memory. Bilateral, well-circumscribed lesions can be created in one or more structures and performance can be evaluated on tasks that are identical or analogous to tasks used in humans. The last decade of the twentieth century saw introduction of functional MRI, PET and SPECT which increased our knowledge of functional anatomy; memory in particular. By conducting a literature search of the material available, this allowed us to identify structures we believe to be involved in spatial memory which are the hippocampus, parahippocampal gyrus, entorhinal cortex and perirhinal cortex.

Memory covers three important aspects of information processing: encoding, storage and retrieval. Any disorder affecting one or more of these stages could result in memory disorder.



There is a debate whether males or females are better at navigation (spatial memory). Two studies published by Piccardi et al in 2011 which included adaptations of known spatial memory tests reported superior male performance. In their first study men were faster than women and required fewer repetitions to learn a path from a map⁷. These sex differences persisted in a subsequent study where women were slower than men in locating a target position⁸. Nevertheless, Silverman and Eals' (1992) work⁹ suggests that females have an advantage regarding the object location memory aspect of spatial memory. Furthermore, McBurney's study¹⁰ based on the well-known game Memory which utilises the cognitive demands required for spatial memory, also supports the female advantage in specific spatial abilities. As the conclusion on the debate is unclear we chose the following aims to explore the subject.

Aims:

- To establish whether there is a difference in spatial memory, T₂ relaxation times of the hippocampus, parahippocampal gyrus, entorhinal cortex and perirhinal cortex and volume estimates of the hippocampus, parahippocampal gyrus between males and females.
- If there is a difference in spatial memory performance, can the difference be explained by T₂ relaxation times or volumes of the hippocampus, parahippocampal gyrus, entorhinal cortex and/or perirhinal cortex.

MATERIAL

RECRUITMENT OF SUBJECTS: The data used in this project was acquired as part of a programme grant entitled “Relationship between lesion location and functional deficits in the amnesic syndrome” awarded to Prof. Andrew Mayes and Prof. Neil Roberts. Volunteers were told the aims and methods of the study, underwent a medical examination and screening for habits and any current or previous conditions related to the nervous, cardiovascular or endocrine systems. All volunteers gave fully informed written consent to participate in the study. Ethics committee approval has been obtained (REC/UL/256-96) prior to the commencement of the study.

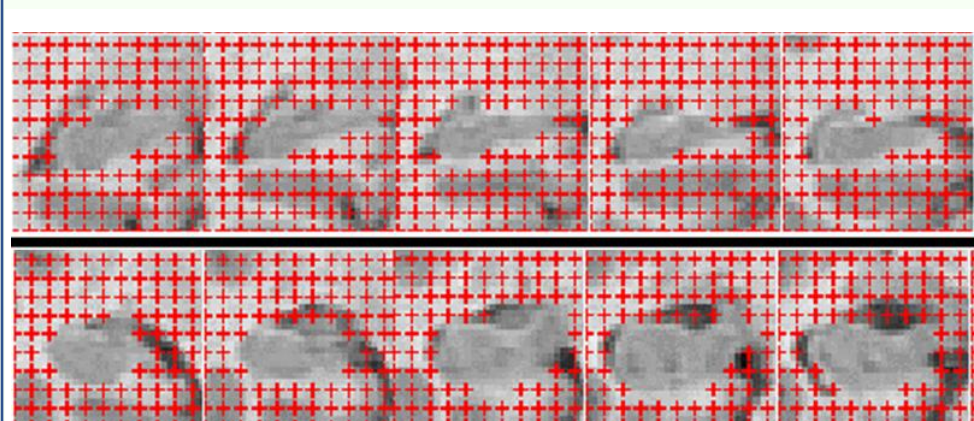
SUBJECT DEMOGRAPHICS: A total of 120 healthy subjects (56 males and 64 females) with a mean age of 50.88±17.74 years (age range: 19-94) are included in the present study.

METHODS

MR IMAGE ACQUISITION: MR imaging was performed at the University of Liverpool Magnetic Resonance and Image Analysis Research Centre, using a 1.5 Tesla MR scanner. The imaging protocol comprised FSE images for the computation of T₂ relaxation times and a T₂-weighted 3D volumetric scan. Subjects were scanned using the quadrature head coil as both transmitter and receiver. Head position was stabilized during the scanning procedure by the use of foam head supports. Following the acquisition of 3D volumetric images, the long axes of the hippocampi were identified on sagittal MR images and 5mm thick slices with 7.5 mm gap between them were prescribed along the hippocampus, perpendicular to its long axis. This prescription maximizes the hippocampal cross sectional area and reduces errors associated with partial voluming. Four images were acquired with a constant TR of 4000 ms and TEs of 30, 45, 75, and 100 ms at 3-5 locations along the hippocampus. With this prescription T₂ relaxation times of hippocampi, parahippocampal gyri, entorhinal and perirhinal cortices were calculated.

VOLUME ESTIMATION

Unbiased estimates of the hippocampus and parahippocampal gyrus were obtained on 3D volumetric images by Cavalieri method of modern design stereology in combination with point counting method using Analyze software¹¹ (Figure 3). Coefficient of error associated with estimates were calculated.



$$Est_V = T \cdot \left(\frac{a}{p} \right) \cdot \frac{1}{M^2} \cdot (P_1 + P_2 + \dots + P_m)$$

$$CE(est_V) = \left(\frac{a}{p} \right)^{-1} \cdot \left\{ \frac{1}{12} \left(3 \sum_{i=1}^m p_i^2 - 4 \sum_{i=1}^m p_i p_{i+1} + \sum_{i=1}^m p_i p_{i+2} \right) + 0.0543 \cdot \frac{B}{\sqrt{a}} \cdot \left(m \cdot \sum_{i=1}^m p_i \right)^{1/2} \right\}^{1/2}$$

$$CE(est_V) = \left(\frac{a}{p} \right)^{-1} \cdot \left\{ \frac{1}{240} \left(3 \sum_{i=1}^m p_i^2 - 4 \sum_{i=1}^m p_i p_{i+1} + \sum_{i=1}^m p_i p_{i+2} \right) + 0.0715 \cdot \frac{B}{\sqrt{a}} \cdot \left(m \cdot \sum_{i=1}^m p_i \right)^{1/2} \right\}^{1/2}$$

Figure 3: Estimation of the volume of the hippocampus using point counting method (Formula 1) and calculation of the precision of the estimation (coefficient of error) for irregular and regular structures (Formulae 2 and 3, respectively)

REFERENCES

- Oxford English Dictionary, <https://www.oed.com>
- Kessels RPC, de Haan EHF, Kappelle LJ & Postma A. (2001). *Brain Research Reviews*, 35, 295-303.
- Ebbinghaus H (1885). *Memory: A Contribution to Experimental Psychology*. Translated by Ruger HA & Bussenius CE (1913).
- Milner B, Corkin S & Teuber HL. (1968). *Neuropsychologia* 6, 215-234.
- Mishkin M (1978). *Nature* 273: 297-298.
- Zola-Morgan S, Squire L & Amaral DG. *Journal of Neuroscience* 6: 1950, 1986
- Piccardi L, Risetti M, Nori R, Tanzilli A, Bernardi L & Guariglia C (2011a). *Learning and Individual Differences*, 21(1), 114-118.
- Piccardi L, Bianchini F, Iasevoli L, Giannone G & Guariglia C. (2011b). *Neuroscience Letters*, 503(3), 181-185.
- Silverman I & Eals M. (1992). In *The adapted mind: Evolutionary psychology and the generation of culture* (pp. 533-549). Barkow JH, Cosmides L, Tooby J (Eds.) Oxford University Press, Oxford.
- McBurney DH, Gaulin SJC, Devineni T, & Adams C. (1997). Superior spatial memory of women: Stronger evidence for the gathering hypothesis. *Evolution and Human Behavior*, 18, 165-174.
- ANALYZE software, MAYO Foundation, Minnesota, USA
- www.mccauslandcenter.sc.edu/crnl/mcricro
- Corballis PM (2003). *Brain and Cognition* 53(2):171-6
- Maguire EA, Nannery R, Spiers HJ. *Brain*. 2006 *Nov*;129(Pt 11):2894-2907

METHODS

T₂ RELAXATION TIME MAPPING: The T₂ relaxation time is calculated on a pixel by pixel basis using log-linear least squares regression analysis. A computer program fits a single exponential to the signal intensity data of corresponding pixels derived from all 4 echoes and constructs an image in which the pixel intensity corresponds to T₂ relaxation time in milliseconds (Figure 4b). ROIs were traced on the processed FSE images and the T₂ relaxation times were calculated using the Region of Interest feature within MRIcro¹². (Figure 5)

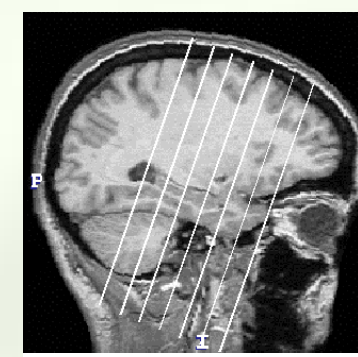


Figure 4a: Location of the slices for the T₂ map

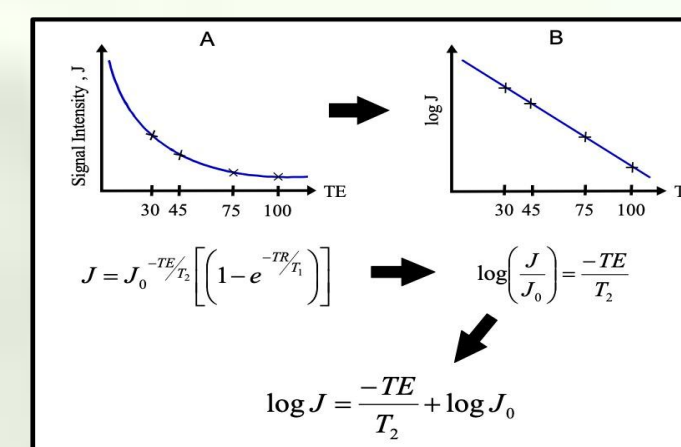


Figure 4b: When a spin echo image with a constant TR is acquired with different TEs, the signal intensities of the images decrease as the TE is increased. If the signal intensity of a pixel is plotted against the TE, the slope of the line can be expressed with the left upper formula where J₀ is the signal intensity at time=0, J is the observed signal intensity at time=t, and e is Napier's constant. If logs of both sides of the equation is taken, the relation between log J and TE is linear and by measuring the slope of this line, it is possible to calculate T₂ relaxation times of different structures

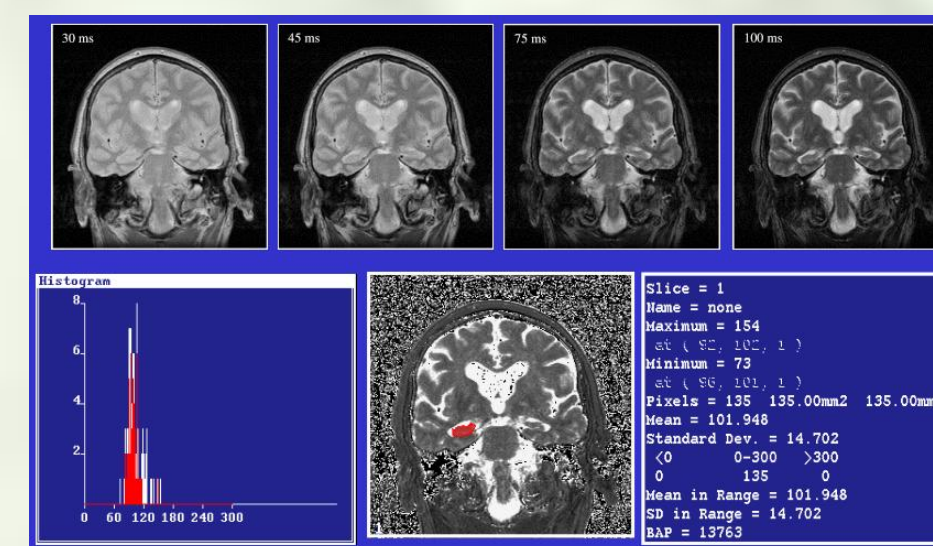


Figure 5: To calculate the T₂ relaxation time of the structure we are interested in e.g. hippocampus, 4 images with differing TEs are acquired (top row). The T₂ mapping algorithm constructs a composite image using the 4 images (bottom middle). The boundary of the hippocampus is traced and the region of interest feature of ANALYZE plots the intensity graph (bottom left) and gives the mean signal intensity, which corresponds to T₂ relaxation time in units of ms., together with other descriptive statistics (bottom right)

MEMORY TESTING

The subjects had a battery of neuropsychological tests, one of which was the Weschler Memory Scale-R. It comprises 11 primary subtests which contribute to 5 major composite scores. We used spatial memory scores.

STATISTICAL ANALYSIS

Data were analyzed using SPSS v24 for Windows (SPSS Inc, Chicago, USA). The distribution of the data was tested by Shapiro-Wilk test. Differences in means of groups were tested by Independent samples T test or Mann Whitney U test, where appropriate. The relationship between spatial memory scores and T₂ relaxation times and volumes were tested by Pearson's correlation analysis. A p value <0.05 was considered significant.

RESULTS

Tables 1, 2 and 3 show the mean volume estimates (coefficient of error); T₂ relaxation times and spatial memory scores of males and females, respectively.

Table 1	Males	Females
Volume estimates, cm3 (CE)		
Right Hippocampus	2.64 (0.43)	2.44 (0.31)
Left Hippocampus	2.53 (0.43)	2.32 (0.29)
Right Parahippocampal gyrus	2.86 (0.62)	2.50 (0.44)
Left Parahippocampal gyrus	2.76 (0.62)	2.41 (0.45)
Table 2	Males	Females
T ₂ relaxation times		
Right Hippocampus	106.22 (5.354)	104.18 (6.513)
Left Hippocampus	108.41 (5.390)	105.95 (5.502)
Right Parahippocampal gyrus	91.84 (4.898)	91.40 (5.511)
Left Parahippocampal gyrus	91.91 (5.212)	93.07 (5.714)
Right Entorhinal cortex	111.65 (9.469)	113.30 (12.405)
Left Entorhinal cortex	110.18 (9.356)	111.38 (9.689)
Right Perirhinal cortex	104.22 (6.064)	103.08 (6.890)
Left Perirhinal cortex	104.14 (6.406)	103.19 (8.107)

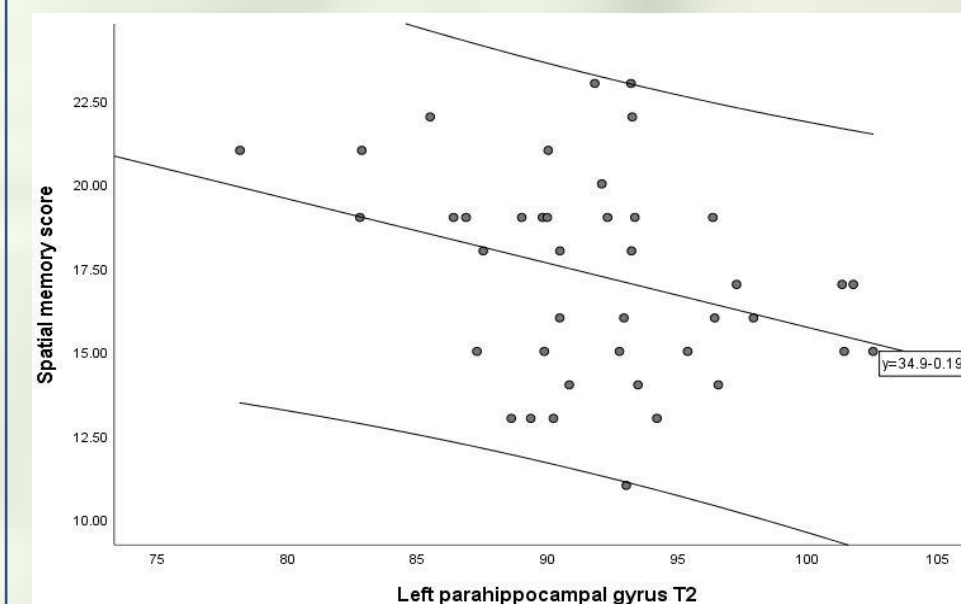
Table 3	Males	Females
Spatial memory score	16.8393 (3.2349)	15.5781 (3.3937)

When the Spatial memory data was analysed by Mann-Whitney U test, the difference between males and females was statistically significant (p=0.019)

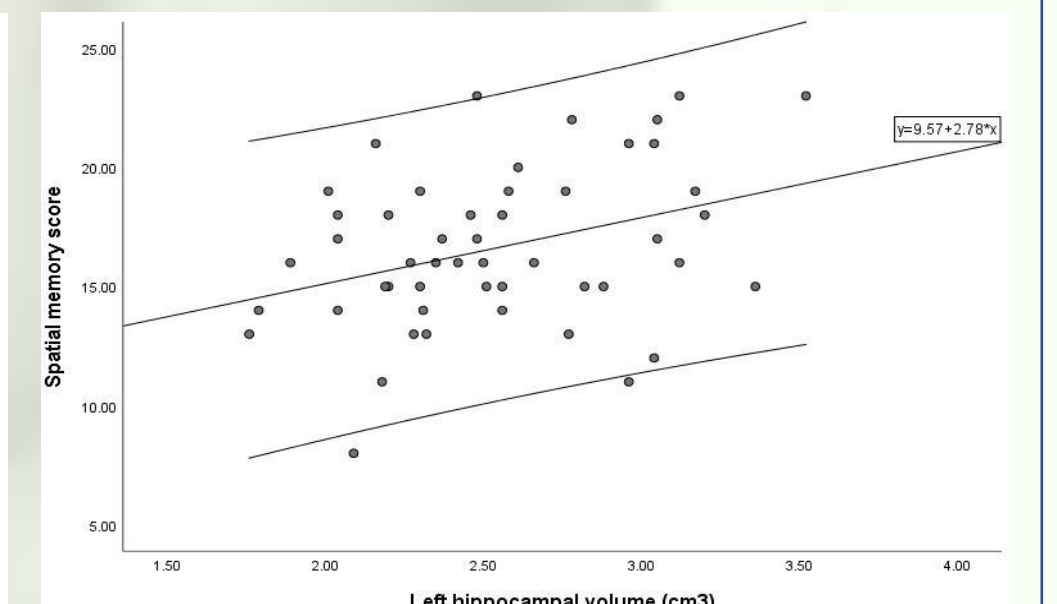
When we examined if the T₂ relaxation times were different between males and females, we found that there were no significant differences.

To establish whether the difference in spatial memory scores between males and females can be attributed to T₂ relaxation times, we conducted correlation analysis. There was a significant correlation between the T₂ relaxation time of the left parahippocampal gyrus and spatial memory score in males (p=0.05) (Graph 1). On the other hand, there was no significant relation between spatial memory score and the T₂ relaxation time of any of the structures in females (p>0.05)

Correlation analysis is repeated for volumes and the spatial memory scores and there was no significant correlation between volumes and the spatial memory scores in females (p>0.05). However, left hippocampal volume correlated significantly with spatial memory score in males (p=0.012) (Graph 2)



Graph 1: Relationship between left parahippocampal gyrus T₂ and spatial memory score in males



Graph 2: Relationship between left hippocampal volume and spatial memory score in males

CONCLUSIONS

In summary, and to answer our question, the neuropsychology data collected indicates that males are better than females at finding their way. There was a significant negative correlation between the T₂ relaxation time of the left parahippocampal gyrus and spatial memory score in males. These relationships may therefore explain why males are better at finding their way around. Low T₂ relaxation time of a structure suggests that the neuron bodies or axons are not replaced, at least significantly by cerebrospinal fluid or glial tissue, an indicator of a healthy state. We also found significant positive correlation between left hippocampal volume and spatial memory score in males.

These findings are rather surprising as structures located in the right, but not the left hemisphere preferentially process information required for functioning visual memory¹³. Activation of the right hippocampus was observed in London taxi drivers, a well-known study group due to their extensive knowledge of streets and routes during spatial memory tasks¹⁴.

Despite these significant findings, the study has its limitations which makes it difficult to draw an accurate conclusion. Firstly, we did not have time for intra- and inter-observer reliability study. Secondly, the MR images on which T₂ was measured were 5 mm thick. Number of slices varied between individuals ranging from 3 to 5 slices and the slice with the optimal view of the structure of interest was used. Measurements on thinner images at standardized locations would be more reliable.

BACKGROUND

Release of Ca²⁺ from the Sarcoplasmic reticulum (SR) is crucial to normal excitation contraction coupling in cardiomyocytes⁽¹⁾. In heart failure, Ca²⁺ release from the SR is unsynchronised causing calcium leak in diastole (relaxation). This leads to diastolic dysfunction and arrhythmias and reduces the SR Ca²⁺ available for the next contraction⁽¹⁾. Physiological levels of intracellular Zn²⁺ has a critical biological role in maintaining normal structure and function of cardiomyocytes. Zn²⁺ homeostasis in the cell is tightly regulated by Zn²⁺ transporters (ZIPs and ZnTs) and Zn²⁺ binding proteins (see figure 1)⁽²⁻³⁾. Zn²⁺ is known to rise in ischemic heart failure and other cardiac myopathies. The Pitt lab has recently shown that Mitsugumin 23 (MG23), a novel Ca²⁺ permeable channel located on the SR is modulated by Zn²⁺⁽⁴⁾. Unpublished data from the lab now reveal that MG23 expression increases when cardiomyocytes are exposed to hypoxia-induced ischemia and that this results in a reduced SR Ca²⁺ content (figure 2)

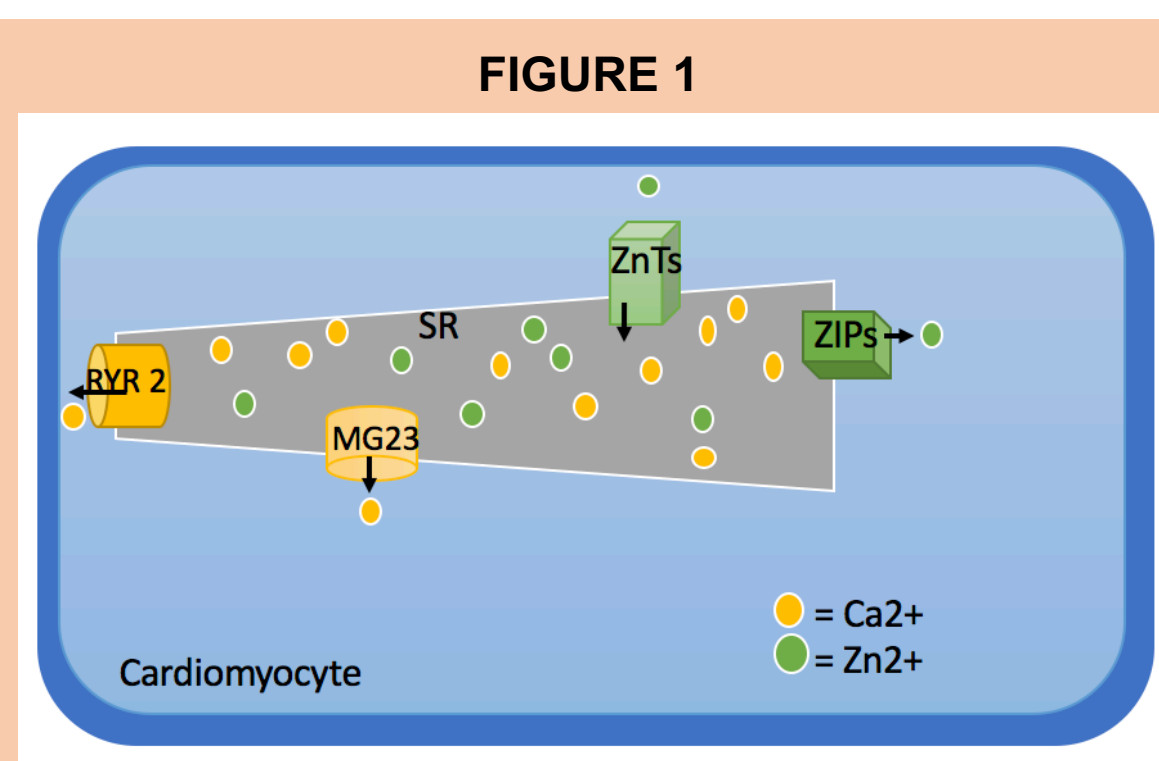


FIGURE 1
Schematic representation of Ca²⁺ channels (Ryanodine Receptor 2 (RyR2) and MG23) and zinc transporters (ZIPs and ZnTs) located on the SR in a cardiomyocyte under physiological conditions.

RESULTS

How does the expression of Zn²⁺ transporters located on the SR change under different hypoxic time points?

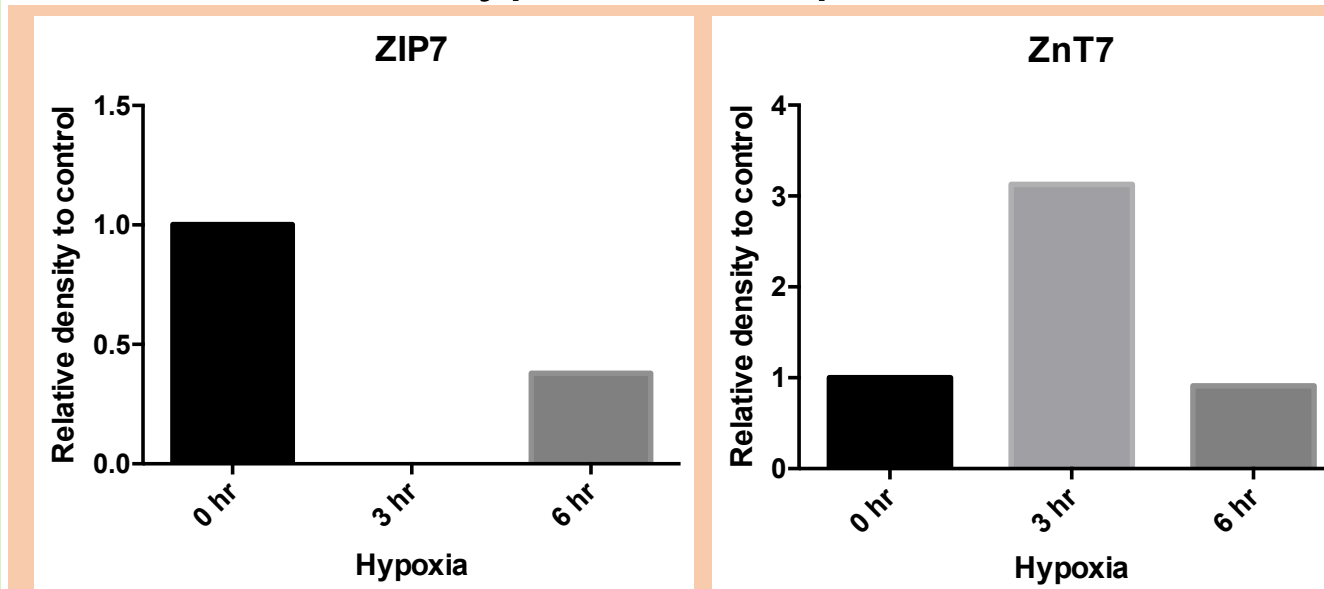


FIGURE 3
Expression of ZIP7 (left) and ZnT7 (right) in cardiomyocytes following 0 hours (control), 3 hours and 6 hours of hypoxia. Anti-ZIP7 at 1:832, anti-rabbit at 1:5000 were used to probe ZIP7 blots whereas anti-ZnT7 at 1:832, anti-rabbit at 1:5000 were used to probe ZnT7 blots.

Is there any re-modelling of RyR2 and SR located Zn²⁺ transporters in MG23 KO heart ?

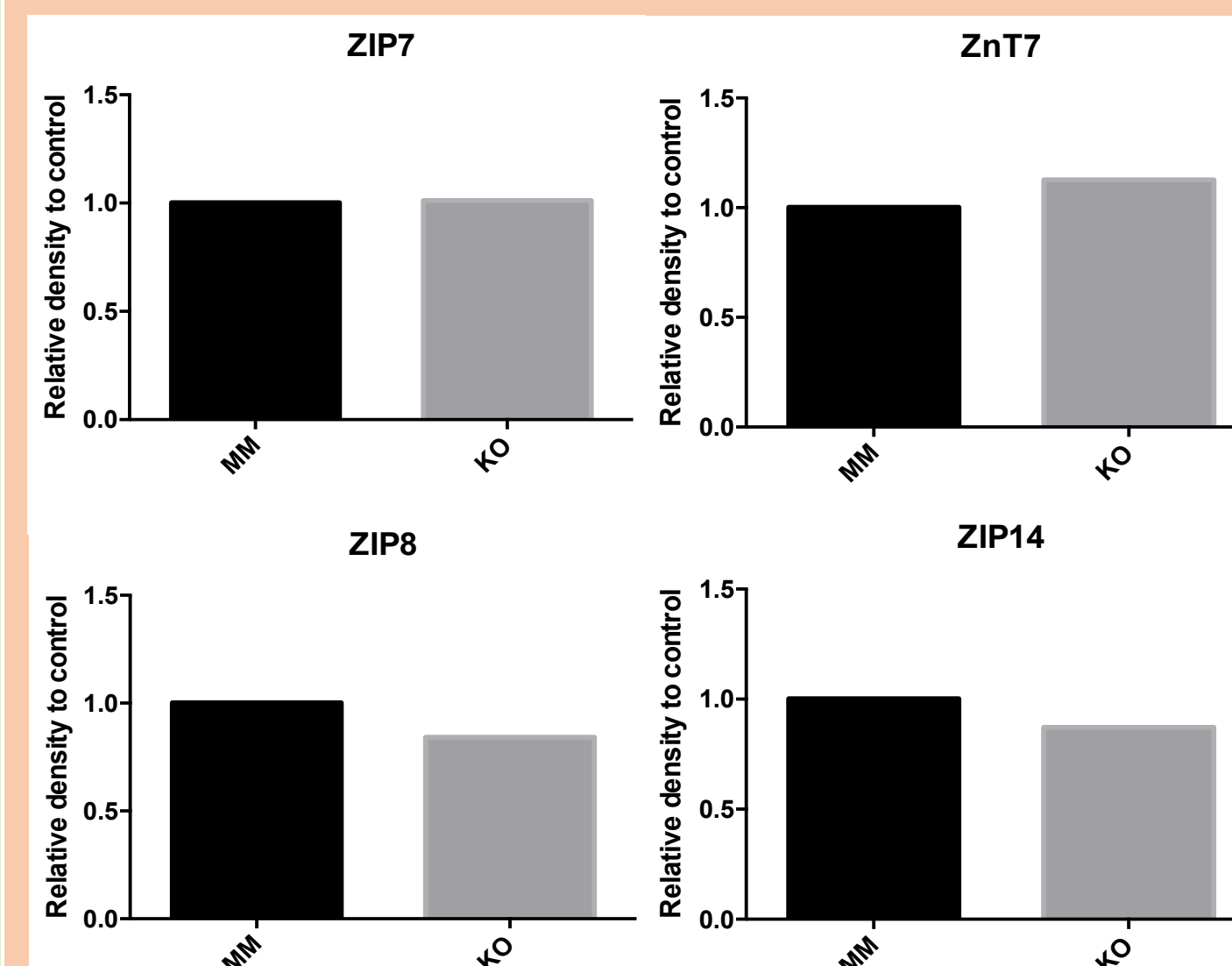


FIGURE 4
Bar charts showing the expression of SR located Zn²⁺ transporters (Clockwise starting top left ZIP7, ZnT7, ZIP8 and ZIP14) in mixed membrane (MM) and MG23 knock out (KO) hearts. Anti-ZIP7, anti-ZnT7, anti-ZIP8, anti-ZIP14 all at 1:832; anti-rabbit at 1:5000 were used to probe the blots.

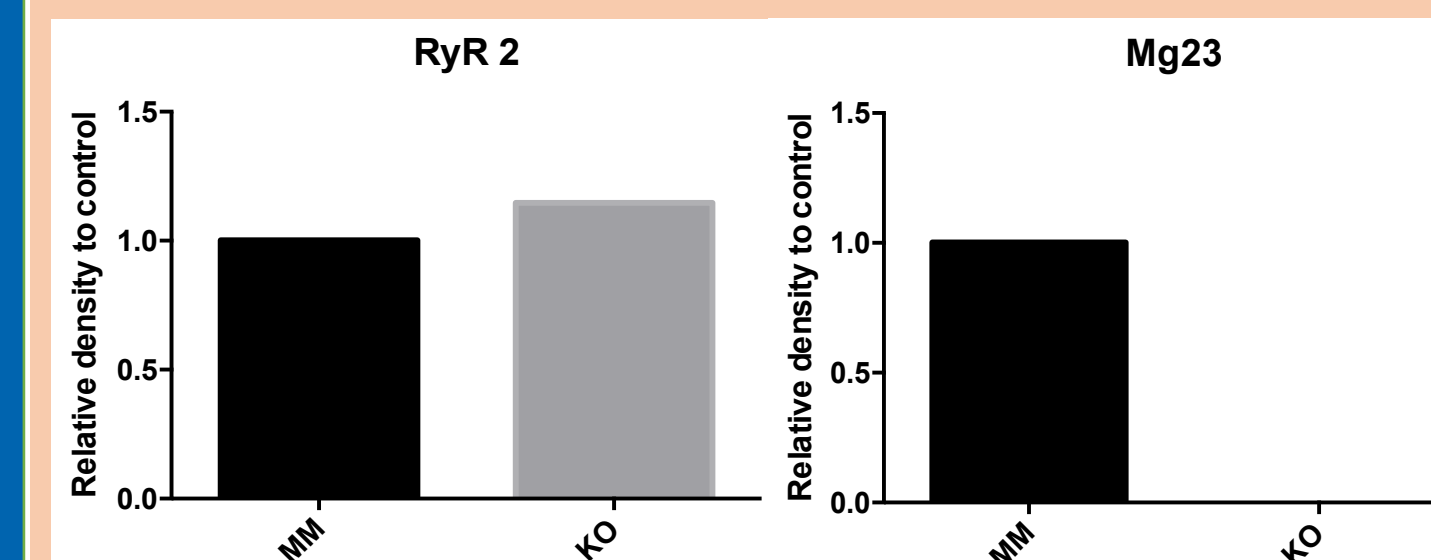


FIGURE 5
Expression profile of Ca²⁺ permeable channels, namely RyR2 (left) and MG23 (right) in mixed membrane (MM) and MG23 knock out (KO) hearts. Anti-RyR2 at 1:1000, anti-mouse at 1:2500 were used to probe RyR2 blot whereas anti-MG23 at 1:5000, anti-rabbit at 1:5000 were used to probe MG23 blot.

CONCLUSION

Following 3 hours hypoxia our data suggest that the cardiomyocyte remodels its SR zinc transporter expression in order to reduce Zn²⁺ levels by pumping Zn²⁺ into the SR and preventing any Zn²⁺ release into the cell. On the contrary at 6 hours hypoxia, the cell can no longer compensate for the overwhelming amount of intracellular Zn²⁺, which sets the cell on a pathogenic pathway. It has been reported that the Zip7 expression decreases while ZnT7 expression increases in heart failure⁽⁵⁾. Hence, it will be interesting to see what happens to the expression of these transporters at higher hypoxic time points. Subtle changes in the expression of RyR and SR located Zn²⁺

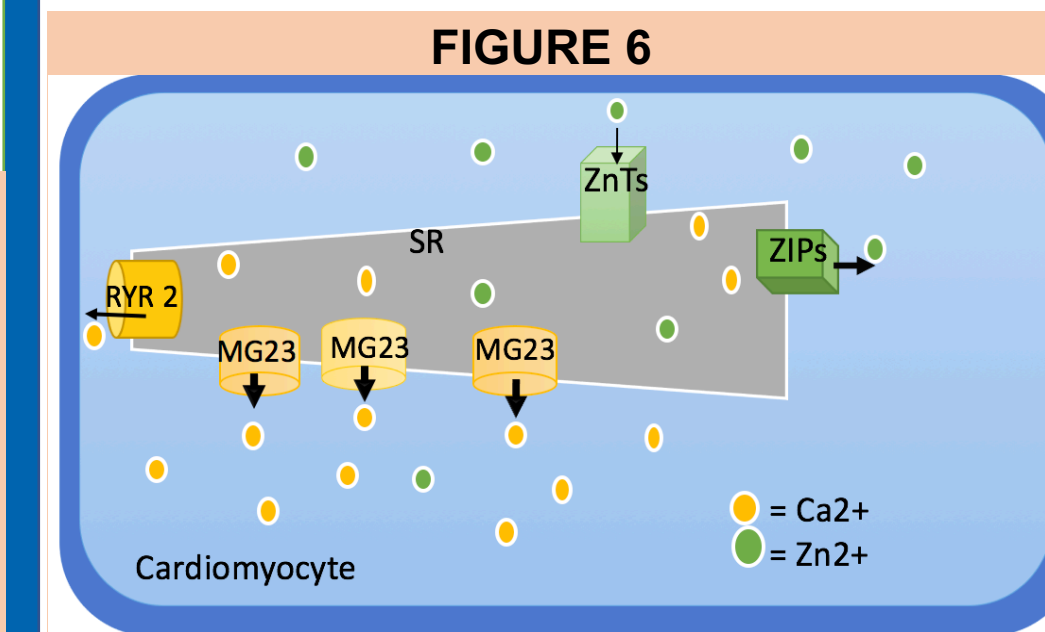


FIGURE 6
Schematic representation of Ca²⁺ channels (RyR2 and MG23) and zinc transporters (ZIPs and ZnTs) located on the SR in a cardiomyocyte under conditions of heart failure.

transporters in MG23 KO heart suggests that the cell does not remodel itself if MG23 is knocked out. The study requires more repeats to be statistically significant but the trends suggest that MG23 could potentially be used as a therapeutic target in heart failure to reduce SR Ca²⁺ leak without altering the activity of RyR2 or other SR located Zn²⁺ transporters.

EXPERIMENTAL PROCEDURE

Western blotting: Lysates were prepared from isolated cardiomyocytes of adult male mice in RIPA buffer. Ethical approval for all animal work was obtained from the University of St Andrews.

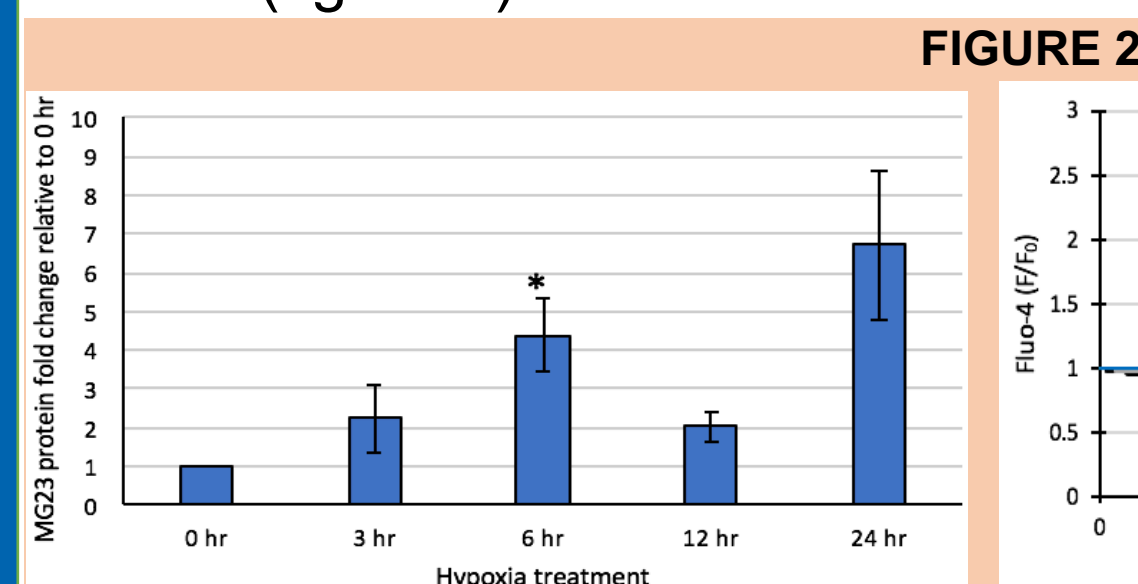
- Protein concentration in the lysates was measured by BCA assay
- 30 µg cell lysate was run on NuPAGE Bis- Tris 4- 12% protein gel at constant current and transferred to a nitrocellulose membrane
- Blocked the membrane and probed it with protein specific primary antibody followed by secondary antibody.
- Imaged using Fuji-film LAS2000 detection system (chemiluminescence)
- Measured density of protein bands using ImageJ software
- Normalised data to loading control, Vinculin and experimental control. Anti-vinculin 1:2500 and anti-mouse 1:5000 were used to probe Vinculin in each case.

REFERENCES

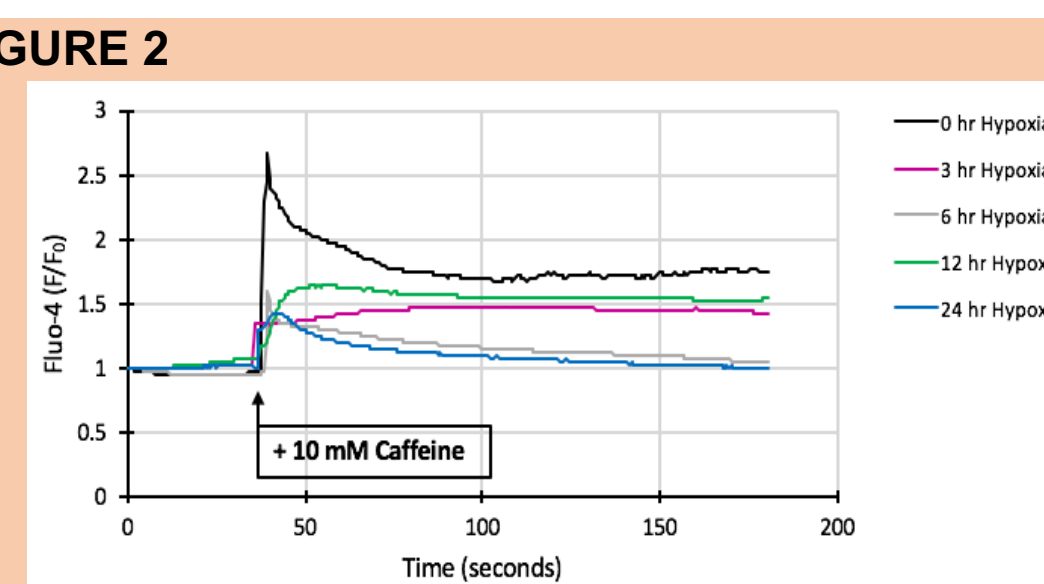
1. Bers, D. M. (2014) *Ann Rev Physiol* 76:107-127
2. Turan, B. and Tuncay, E. *Int. J. Mol. Sci.* 2017, 18(11), 2395
3. Bodiga, V. L., Thokala, S. and Kovur, S. M. *Biol Trace Elem Res* (Sep 2017): 179(1):117-129.
4. Donnell, B.R., Robertson GB, Karumbi A, McIntyre C, Bal W, Nishi M, Takeshima H, Stewart AJ, Pitt SJ. *J Biol Chem.* 2017 Aug 11;292(32):13361-13373.
5. Belma Turan, *Biophys. J.*: 2656-PosB263 February 2017

KEY FINDINGS

- In cardiomyocytes Zip7 expression is suppressed on exposure to 3 hours of hypoxia, but at 6 hours of hypoxia its expression increases to almost 50% of control.
- At 3 hours of hypoxia, ZnT7 expression elevates by 3 folds, whereas at 6 hours hypoxia its expression declines to almost the level of the control.
- Subtle changes in the expression of RyR2 and SR located Zn²⁺ transporters in MG23 KO heart are noted.



2(a) Increase in MG23 protein expression in mouse cardiomyocytes on exposure to hypoxic conditions (0.5% O₂). *p<0.05, n= 3 hearts per condition



2(b) On addition of 10mM of caffeine (RyR2 Agonist) to mouse cardiomyocytes following hypoxia, Ca²⁺ release from the SR decline significantly at increased hypoxic time points.

HYPOTHESIS and AIMS

Zn²⁺ dyshomeostasis plays a role in dysregulated intracellular Ca²⁺ release. Our current hypothesis is that in hypoxia SR Zn²⁺ transporters and Ca²⁺ channels are remodelled which contribute to pathophysiological cellular Zn²⁺ and Ca²⁺ dynamics.

The aims of the study were to:

- (1) Determine the expression profile of Zn²⁺ transporters located on the SR under different hypoxic time points,
- (2) Determine the expression profile of RyR2 and SR located Zn²⁺ transporters in MG23 knock out (KO) heart.

HOW DO MEDICAL STUDENTS MANAGE STRESS AND WHAT ROLE DOES MEDICAL EDUCATIONAL ENVIRONMENT PLAY IN THE EXPERIENCE OF STRESS?

WEI QIAN ONG, GOZDE OZAKINCI, ANITA LAIDLAW

BACKGROUND

- Burnout is defined as the experience of emotional exhaustion, cynicism and lack of professional efficacy⁽¹⁾.
- This may lead to poorer quality of patient care, decreased empathy and emotional instability for future physicians⁽²⁾.
- Furthermore, research also suggests that these physician burnout symptoms may present as early as medical school⁽³⁾.
- Hence, it is essential to measure and understand the factors that contribute to stress and burnout, especially in the context of medical school environment, as well as the coping strategies that may promote resilience against burnout, so that relevant resources and support can be offered to students to look after their own wellbeing and health.

METHODS

- The study was conducted 18 June – 22 July 2019. Undergraduate medical students of the University of St Andrews, University of Dundee and University of Aberdeen were recruited via recruitment posters, Facebook pages and University email newsletters for an online survey.
- This study was approved by the University of St Andrews School of Medicine Ethics Committee (UTREC Approval Code: MD14339).
- The survey measured the participant's demographic profile, and assessed their perception of their medical school environment, competitiveness, levels of burnout and perceived stress, as well as their coping strategies by using the following scales:
 1. Demographic questionnaire
 2. Dundee Ready Education Environment Measure (DREEM)
 3. Personal Development Competitive Attitude Scale (PDCA)
 4. Oldenburg's Burnout Inventory (OBI)
 5. Perceived Stress Scale (PSS4)
 6. Brief Coping Inventory
- The following hypotheses were tested:
 - Better perception of the medical school environment → Lower levels of stress/burnout
 - More competitive → Lower levels of stress/burnout
 - Better coping strategies → Lower levels of stress/burnout

RESULTS

- 198 students (57 males, 141 females) participated in the study. The participants' age ranged from 18 to 32, with a mean age of 21.32 ± 2.56. The significant correlation of both stress and burnout with the other scales are shown below:

SCALE	PEARSON CORRELATION (STRESS)	PEARSON CORRELATION (BURNOUT DISENGAGEMENT)	PEARSON CORRELATION (BURNOUT EXHAUSTION)
DREEM (Academic Self-Perception)	-0.36	-0.49	-0.43
DREEM (Perception of Atmosphere)	-0.44	-0.66	-0.39
DREEM (Social Self-Perception)	-0.54	-0.60	-0.53
PDCA	-0.29	-0.28	-0.32
Brief COPE (Self Distraction)	0.18	0.17	0.17
Brief COPE (Denial)	0.33	0.24	0.22
Brief COPE (Venting)	0.21	0.21	0.29
Brief COPE (Behavioural Disengagement)	0.42	0.34	0.44
Brief COPE (Self Blame)	0.52	0.41	0.47



Negatively correlated with DREEM



Negatively correlated with PDCA

HELP!

Positively correlated with Brief COPE Self Distraction, Denial, Venting, Behavioural Disengagement and Self Blame subscales

DISCUSSION

- This study focused on students' perception of their medical school environment, individual competitiveness, as well as coping strategies against self-perceived levels of stress/burnout.
- As hypothesised, the better the students' self-perception of their medical educational environment, the lower their levels of reported stress and burnout.
- Students that scored higher on the PDCA score also reported lower levels of stress and burnout as expected, as individuals that score higher in the PDCA scale tend to be lower in neuroticism and higher in personal and social self esteem⁽⁴⁾.
- Students who have reported higher levels of stress and burnout were found to use self distraction, denial, venting, behavioural disengagement and self blame as coping strategies against stress.
- In the future, more attention should be given to improve students' medical school educational experience, identify individual student's competitiveness as well as their coping strategies so that more help could be offered to reduce students' stress and burnout and promote a better overall physical, mental and emotional wellbeing.

REFERENCES

1. Maslach C, Jackson S. The measurement of experienced Burnout. *Journal Of Occupational Behaviour*. 1981; 2: 99–113. Available from: <https://doi.org/10.1002/job.4030020205>
2. Ghetti C, Chang J, Gosman G. Burnout, Psychological Skills, and Empathy: Balint Training in Obstetrics and Gynecology Residents. *Journal of Graduate Medical Education*. 2009; 1(2): 231–235. Available from: DOI: 10.4300/JGME-D-09-00049.1
3. Dyrbye LN, West CP, Satele D, Boone S, Tan L, Sloan J, Shanafelt TD. Burnout among U.S. medical students, residents, and early career physicians relative to the general U.S. population. *Academic Medicine*. 2014; 89(3): 443–451. Available from: DOI: 10.1097/ACM.000000000000134
4. Ryckman, RM, Hammer, M, Kaczor, LM, Gold, JA. Construction of a personal development competitive attitude scale. *J. Pers. Assess.* 1998; 66: 374–385. DOI: 10.1207/s15327752jpa6602_15



I. Introduction

A family of neuropeptides called kisspeptins drive reproductive hormone secretions from the brain to control fertility. Kisspeptins are found in anatomically distinct cell populations in the limbic brain where each population regulates a particular aspect of reproductive physiology, including triggering ovulation and controlling sex steroid levels to maintain sperm and follicle development. Each population functions through a complex array of molecular mechanisms, however, the unique gene expression signatures of each population remain unknown. By using novel transgenic mouse models combined with viral targeting tools we determined the global gene expression profiles of kisspeptin neurone populations in the rostral periventricular region of the 3rd ventricle (RP3V), the arcuate nucleus (ARC) and the medial amygdala (MeA) under different conditions of sex hormone feedback. This allows us to catalogue the transcriptome-wide events underlying this key nodal network that controls the reproductive brain.

2. Methods

- We utilised a line of female transgenic mice where Cre recombinase is expressed specifically in kisspeptin neurones [1]. These mice were injected with a Cre-dependent adenoassociated virus vector (AAV) encoding a Ribo-Tagging cassette targeting 3 sites (RP3V, ARC and MeA) bilaterally.
- 3 weeks post-injection, the ovarian stage of each mouse was assessed and mice were culled at either proestrus or diestrus. Brains were rapidly removed and tissue surrounding each of the three kisspeptin populations was excised.
- Using immunofluorescence labelling, we verified the Ribo-Tag AAV delivered haemagglutinin-tagged ribosomes to kisspeptin neurones.
- Messenger RNA from actively transcribing ribosomes was isolated using an anti-haemagglutinin antibody and used to prepare cDNA libraries for each neuronal population.
- The gene expression profiles from kisspeptin neurones from the RP3V, ARC and MeA were then analysed and quantified by qPCR utilising candidate gene primers.

Methods Continued

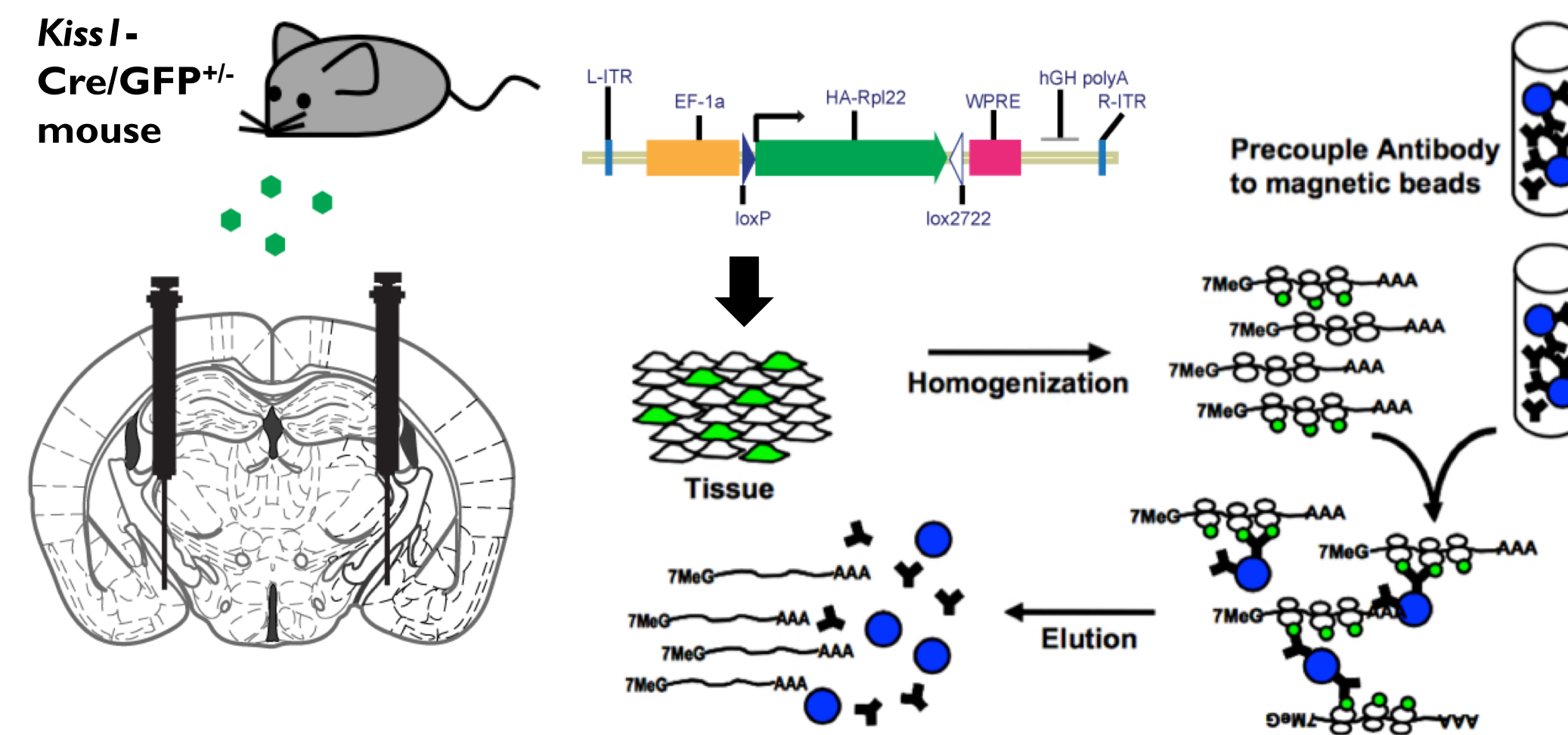


Fig 1. *Kiss1-Cre/GFP* transgenic mouse line used and diagram representing MeA injection sites of viral vector. Figure adapted from [2].

Fig 2. Ribo-Tagging procedure adapted from [3]. Viral vector injected into the brain is activated by Cre-recombinase. Ribo-Tagging procedure utilised to isolate mRNA-ribosome complexes from kisspeptin neurones

Results Continued

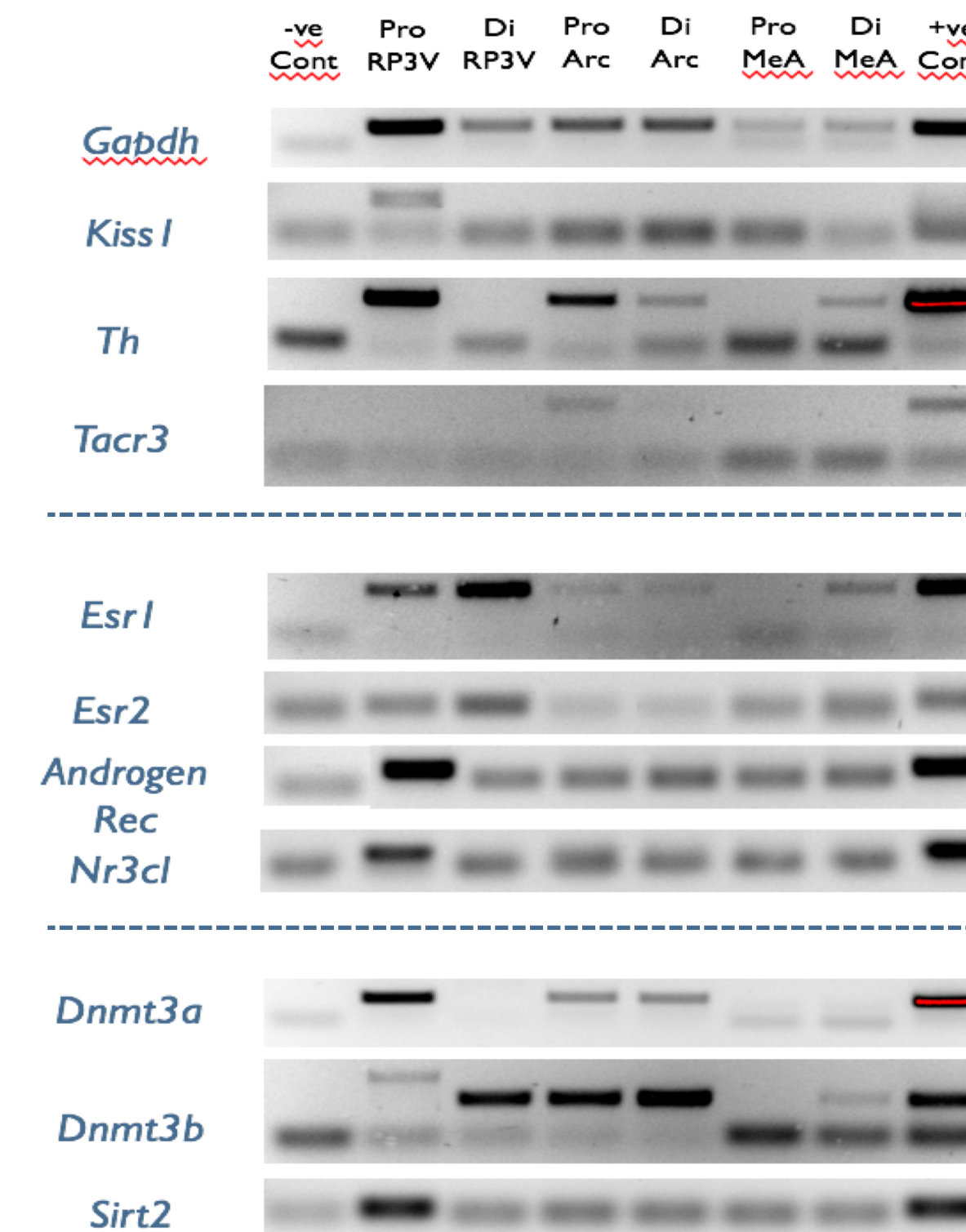


Fig. 6. RT-PCR expression profiles of various neuroendocrine genes of interest. Gene profiles of differentially expressed transcripts were identified from discrete kisspeptin neurone populations. Some gene expression patterns validated current scientific literature, whereas others were novel

3. Results

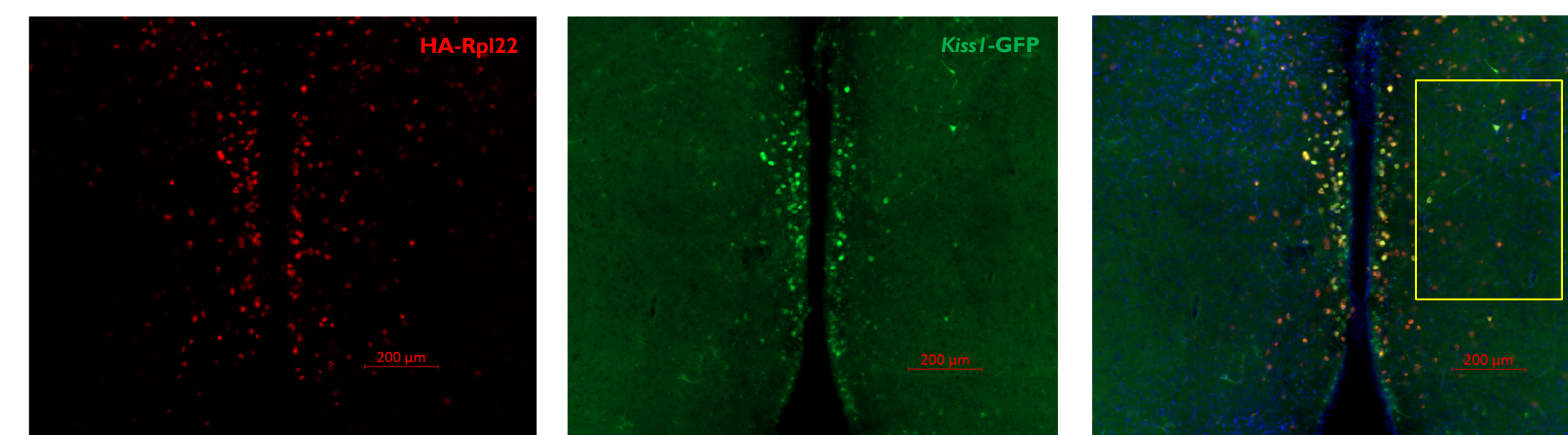


Fig 3. Images showing cells labelled with anti-HA and *Kiss1*-neurone-expressed GFP

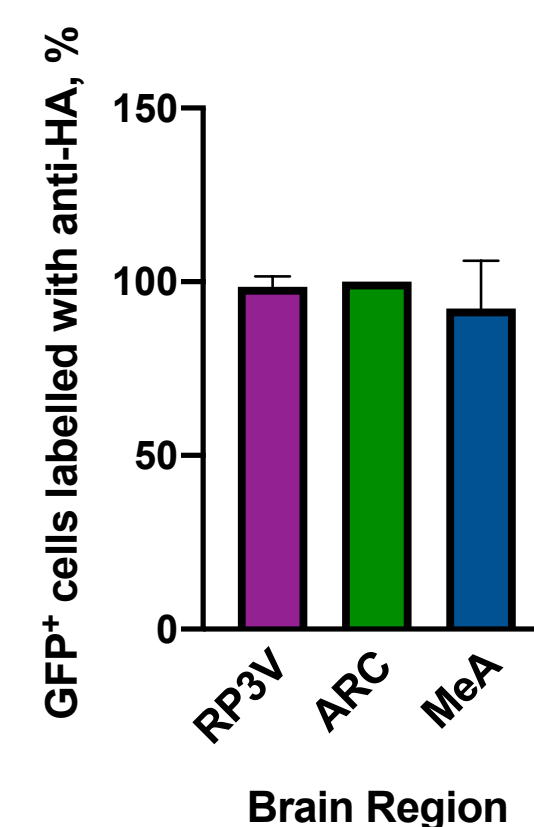


Fig 4. The co-expression of green fluorescence labelled kisspeptin neurones and HA-Rpl22 in different brain nuclei

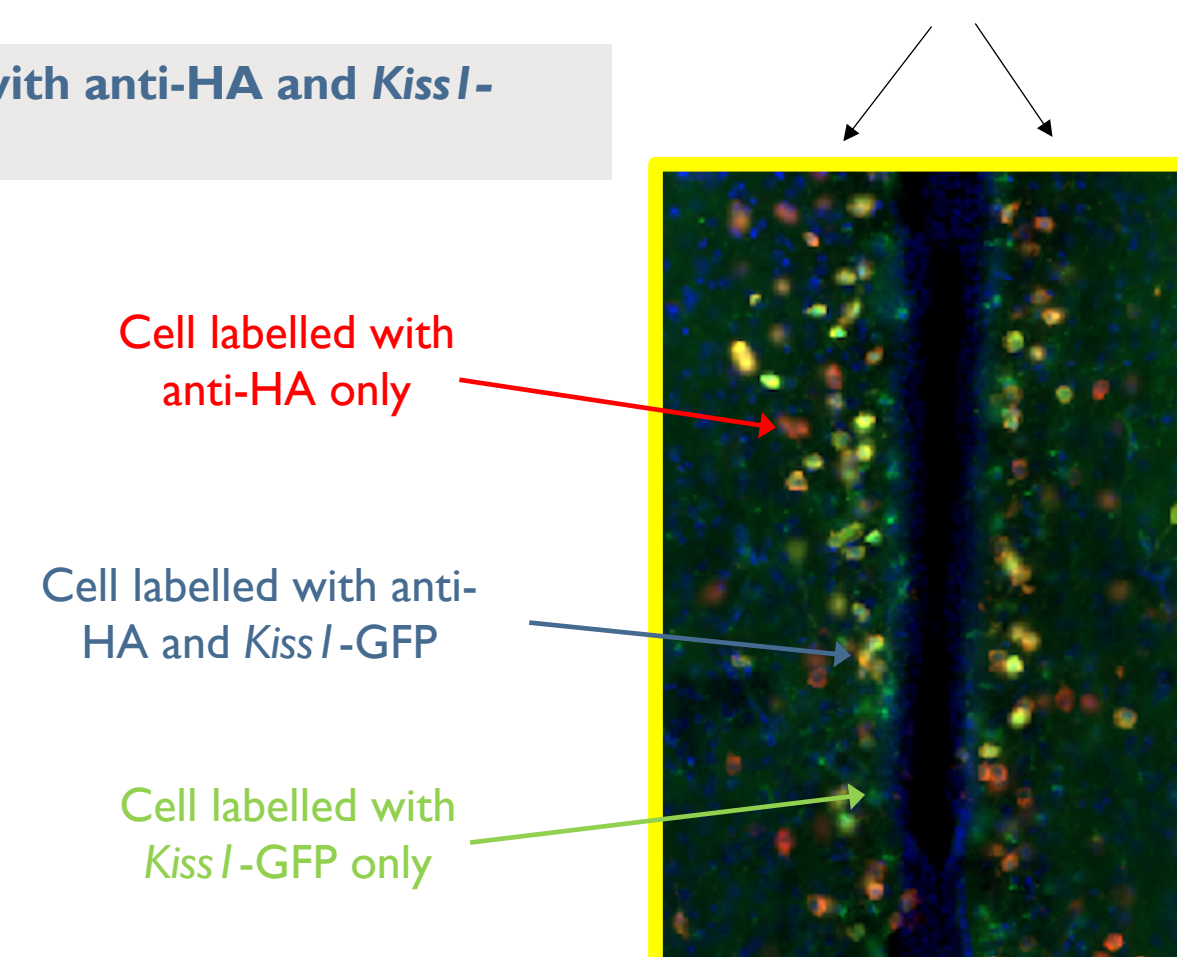


Fig 5. Enlarged micrograph showing cells expressing HA-Rpl22, *Kiss1*-GFP or both

Conclusion

- Gapdh* gene expression was found in all cDNA libraries confirming our ability to isolate ribosome-associated mRNA.
- Kiss1* expression was consistent with the scientific literature being highest in the RP3V population taken at proestrus
- Analysis of *Th* expression confirmed that RP3V *Kiss1* neurons have dopaminergic properties.
- Analysis of sex steroid receptor expression including *Esr1*, *Esr2* and *Ar* confirms that *Kiss1* neurons have the ability to relay the effects of many circulating steroids.
- Expression of the glucocorticoid receptor (*Nr3c1*) was detected in RP3V *Kiss1* neurons, suggesting these neurons may be directly responsive to stress signals.

This project reveals the gene expression profiles from discrete Kiss1 neuronal populations using a cutting-edge Ribo-Tagging procedure. My results provide an exciting foundation from which further research can be performed into how each kisspeptin neuronal population can sense and integrate molecular signals to control the reproductive brain or identify how they integrate with other physiological processes.

References

- Gottsch et al. (2011). *Endocrinology* **152**, 4298-4309.
- Sanz et al. (2015). *JNeurosci* **35**, 5549-5556.
- Sanz et al. (2009). *PNAS* **106**, 13939-13944.

Chen, W.H., Elshani, M., Kudsy, M., Um, I.H., Mullen, P. & Harrison, D.J.

INTRODUCTION

- Renal cell carcinoma (RCC) is the 16th most frequent cause of death around the world (Znaor et al., 2015).
- RCC tends to be highly vascularised and immunogenic with a very adaptive and heterogenous tumour microenvironment (Heidegger et al., 2019).
- ProTide Drug NUC-7738 is a cordycepin analogue. Cordycepin has been shown to down-regulate cell proliferation and growth, induce tumour apoptosis (Jin et al, 2018). It has also been shown to affect the tumour microenvironment (TME), inhibiting the migration and invasion of tumour cells as well as disrupting interactions between the tumour and its surrounding stromal cells.
- This experiment will test the efficacy of ProTide Drug NUC-7738 on RCC while considering factors reflective of in vivo conditions. These factors include tumour heterogeneity and the tumour's interaction with its microenvironment.

RESULTS

pAMPK EXPRESSION

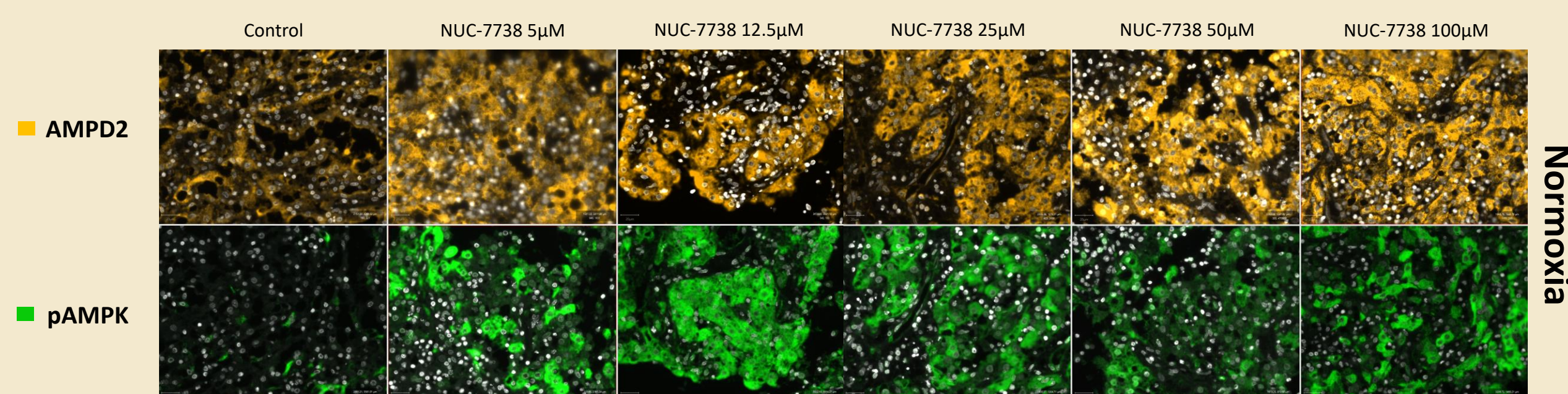


Figure 1. Visualisation of proteins AMPD2 and pAMPK using immunofluorescence. It can be observed that pAMPK levels were raised throughout all the concentrations of NUC-7738 even in the presence of AMPD2.

CLEAVED CASPASE 3 EXPRESSION

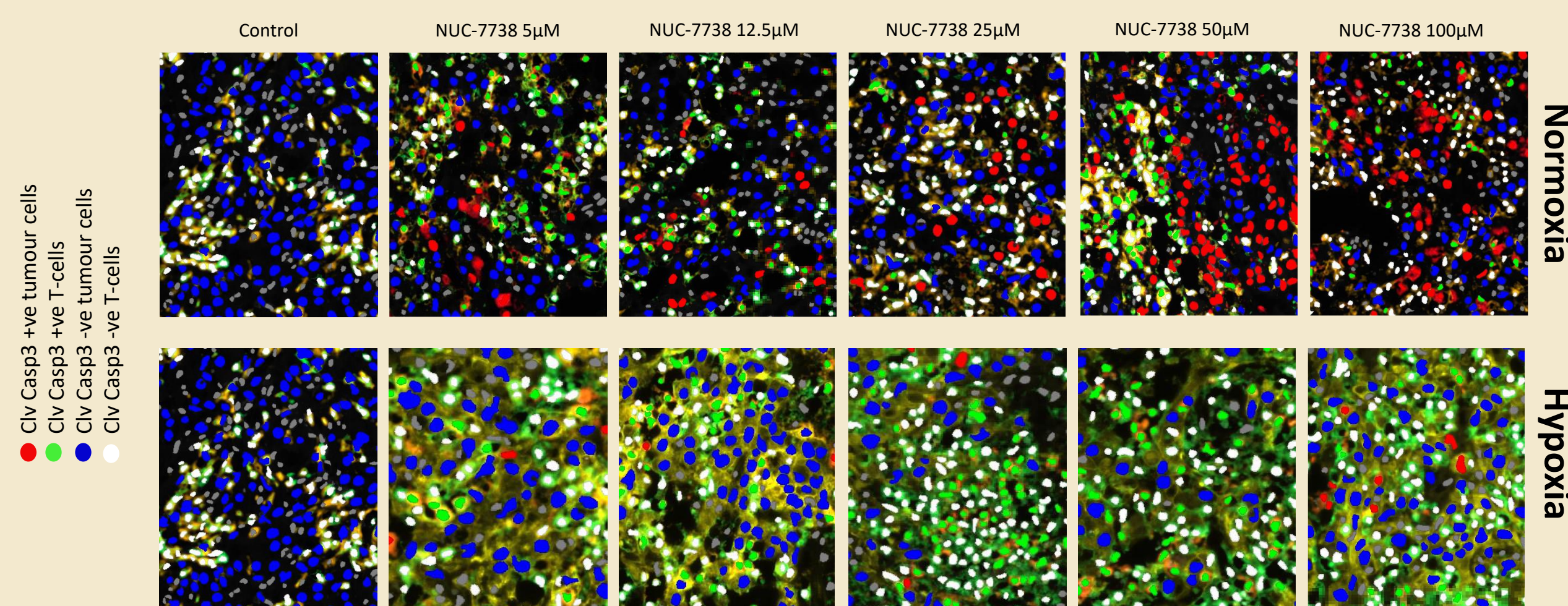


Figure 2. Visualisation of proteins cleaved caspase 3, CD3, CD8 and pan cytokeratin using immunofluorescence with an overlay of 4 colours (legend to the left) achieved using QuPath to classify the cells visualised in this image.

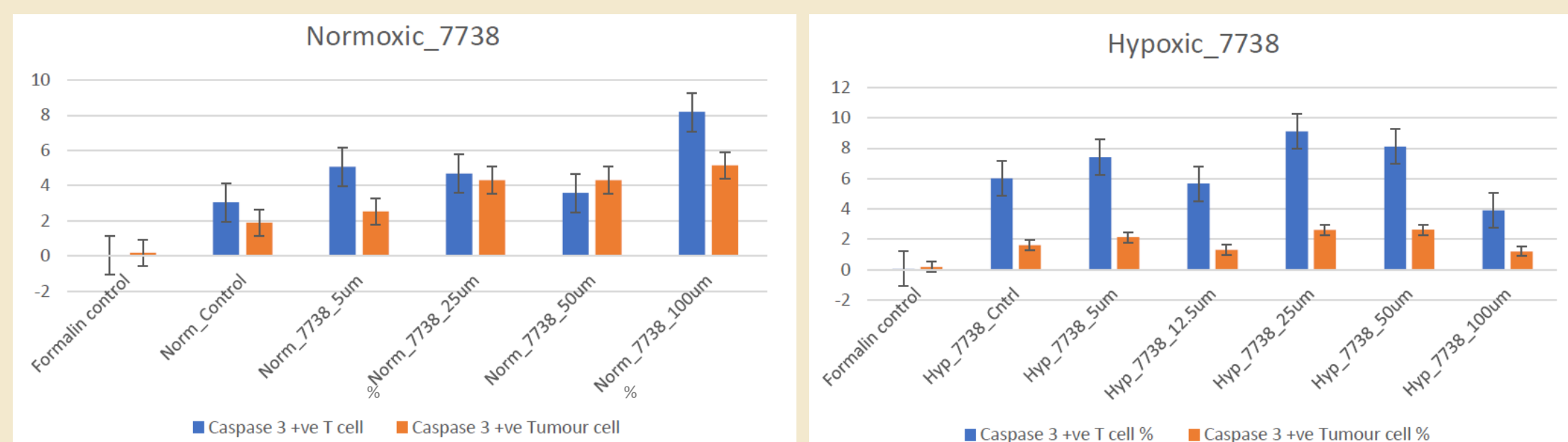


Figure 3. Dynamite plots of the percentages of cleaved caspase 3 positive T-cells and tumour cells in both normoxic and hypoxic conditions.

Together, Figures 2 and 3 show that the percentage of cleaved caspase 3 positive (indicative of apoptosis) tumour cells and T cells increased with the increasing concentrations of drug in normoxic conditions.

The percentages of cleaved caspase 3 positive T-cells were generally higher in hypoxic conditions than in normoxia, whilst the opposite was true for tumour cells.

REFERENCES

- Heidegger, I., Pircher, A. and Pichler, R. (2019). *Targeting the Tumor Microenvironment in Renal Cell Cancer Biology and Therapy*. Available at: <https://www.frontiersin.org/articles/10.3389/fonc.2019.00490/full#F1> [Accessed 19 August 2019].
- Jin, Y., Meng, X., Qiu, Z., Su, Y., Yu, P. & Qu, P. (2018). *Anti-tumor and anti-metastatic roles of cordycepin, one bioactive compound of Cordyceps militaris*. Saudi Journal of Biological Science, 25(5). Available at: <https://www.sciencedirect.com/science/article/pii/S1319562X1830127X?via%3Dihub> [Accessed 30 August 2019].
- Schöning, J., Monteiro, M. and Gu, W. (2017). Drug resistance and cancer stem cells: the shared but distinct roles of hypoxia-inducible factors HIF1 α and HIF2 α . *Clinical and Experimental Pharmacology and Physiology*, 44(2), pp.153-161.
- Znaor, A., Lortet-Tieulent, J., Laversanne, M., Jemal, A., & Bray, F. (2015). *International Variations and Trends in Renal Cell Carcinoma Incidence and Mortality*. *European Urology*, 67(3), 519–530. doi:10.1016/j.eururo.2014.10.002.

AIMS

- To observe the effects of ProTide Drug NUC-7738 on RCC and its microenvironment, more specifically, its immune tumour microenvironment.
- To observe if there are any differences in results gained from in vitro studies and this ex vivo study.

METHODS

- Primary human RCC was collected immediately after a nephrectomy. A portion of the collected tissue was immediately fixed in formalin to serve as a control.
- The tissue was sliced into 250 μ m slices using a vibratome.
- Individual slices were treated in different drug concentrations (control, 5 μ M, 12.5 μ M, 25 μ M, 50 μ M, 100 μ M) for 24 hours. One set of drug concentrations were treated in normoxic conditions and another in hypoxic (0.05% O₂) conditions.
- After treatment, slices were fixed in formalin and subsequently embedded in paraffin.
- 3 μ m slices were cut out of the paraffin blocks and placed on slides.
- The slides were stained with multiple fluorophores to visualise co-expression of proteins on the same tissue slice. The immunofluorescent stains were grouped as follows:

Set 1	Set 2
<ul style="list-style-type: none"> • Cleaved caspase 3 • pAMPK • AMPD2 • Pan cytokeratin • DAPI 	<ul style="list-style-type: none"> • Cleaved caspase 3 • CD3 • CD8 • Pan cytokeratin • CA9

- Slides were then visualised under ZEISS Axio Scan.Z1
- Images of the slides were processed through a bioimage analysis software QuPath, to classify the different types of cells and quantify the percentage that expressed cleaved caspase 3.

CONCLUSIONS

- Results suggest that NUC-7738 does indeed affect the AMPK signalling pathway, increasing the levels of pAMPK.
- While initially postulated that AMPD2 would metabolise the active form of NUC-7738 hence decreasing the efficacy of the drug, this does not seem to be the case. This result, while initially unexpected, has been reproduced in in vitro studies, indicating that this tumour response is unlikely to be due to the ex vivo conditions.
- In normoxic conditions, results suggest that NUC-7738 triggers apoptosis in tumour cells at concentrations of 25 μ M and higher and in T-cells at 100 μ M and higher, showing promise of its effectiveness as an anti-cancer drug.
- Hypoxia seemed to trigger an increased rate of apoptosis in T-cells while a lower rate in tumour cells. This could be because the lower oxygen levels were not conducive for T-cells survival whilst Schöning et al. (2016) suggest that hypoxia causes some tumour cells to go into a quiescent state, reducing efficacy of the drug.
- This experiment should be repeated with a longer treatment time (48h) and less harsh hypoxic conditions to assess the utility of this ex vivo testing.

Background

Renal cell carcinoma (RCC) is the eighth most common cancer in the UK, with over 44% of all cases detected at stages III or IV due to often asymptomatic early disease (1). Prognosis in late stage disease is especially poor, so the advent of glutaminase inhibitors presents a novel opportunity to improve patient outcomes. Metabolic reprogramming is an emerging hallmark of cancer, with translation into the clinic in its nascentcy. RCC differs from healthy tissue in that glutamine, rather than glucose, is the primary substrate for respiration. This is sometimes termed 'glutamine addiction' or the Warburg Effect. Drug resistance is a common obstacle faced by patients with cancer, and RCC is no exception. We hypothesise that CB-839 shows synthetic lethality when in combination with Drug X. The primary goal of this project is to investigate possible synergy between CB-839 and Drug X. With better understanding of mechanisms underpinning resistance to glutaminase inhibitors it may be possible to enhance the drug's clinical efficacy, with potential for translation into improved patient outcomes.

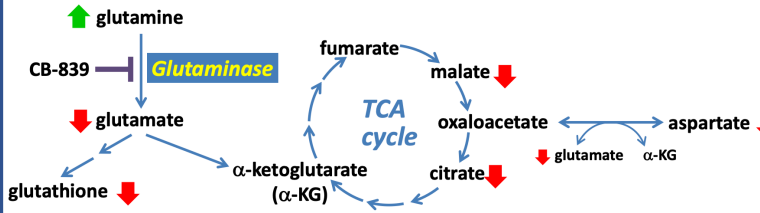
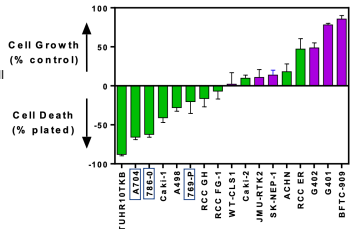


Figure 1 (left)
Diagram showing metabolism of glutamine into glutamate via glutaminase enzyme. See CB-839's inhibition of glutaminase and effects on the metabolic pathway, (adapted from 2)

Figure 2 (right)
Graph indicating levels of intrinsic resistance to CB-839 in different renal cell carcinoma cell lines. This informed selection of cell lines for the project. (3)



Materials

CB-839 (Telaglenastat)

CB-839 is an example of an emerging drug class, aiming to reprogram metabolism in cancerous cells. The drug exploits glutamine addiction, a hallmark of renal cell carcinoma, enabling selective toxicity. CB-839 is an allosteric inhibitor of glutaminase, currently in phase II clinical trials (4).

Drug X

Drug X affects actin cytoskeletal dynamics. Given actin's integral role in cytoskeleton integrity, Drug X disrupts cell polarity, migration and cytokinesis (5).

Renal Cell Carcinoma Cell Lines

3 cell lines of clear cell renal cell carcinoma (ccRCC) were used: 786-0, 769-P and A704. Each line was cultured in either minimum essential media (MEM) or RPMI, representing physiological or diabetic blood glucose concentrations respectively.

Methods

Each cell line was treated with CB-839 and Drug X separately in order to establish baseline effects of each drug and to quantify IC50 values. IC50 is a measure of the concentration of drug required to reduce growth by 50%. 786-0 RPMI and 769-P RPMI lines were later exposed to combinations of the 2 drugs.

Cells were aliquoted onto flat bottomed 96 well plates at the desired seeding density, followed by 24 hour incubation at 37°C. Following this, cells were treated with drug. Treated cells were then incubated for 72 hours, also at 37°C, after which time they were fixed with TCA. A Sulforhodamine B assay (SRB) was then started in order to quantify growth of cells.

SRB is colorimetric assay used to quantify the percentage survival of cells through staining and measurement of light absorbance (570nm). (4)

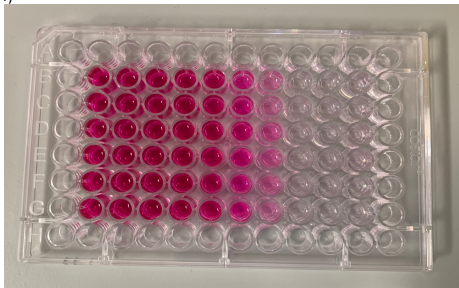


Figure 3
96 well plate of 786-0 RPMI, treated with Drug X, SRB assay in progress. Intensity of purple stain indicates confluency of cells.

Results

Survival Curves for CB839

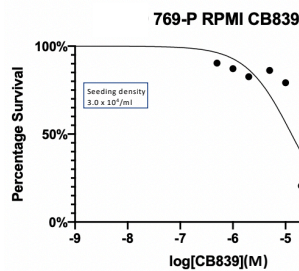


Figure 4a
Graph of percentage survival of 769-P RPMI against concentration of CB-839. Inhibition of growth was observed over a range of concentrations, spanning 0.5-100µM.

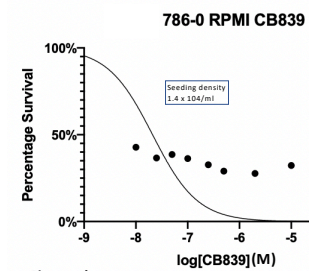


Figure 4b
Graph of percentage survival of 786-0 RPMI against concentration of CB-839. Inhibition of growth was observed over a range of concentrations, spanning 0.01-100µM.

Survival Curves for Drug X

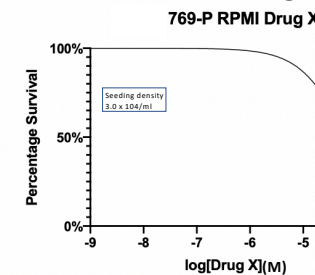


Figure 5a
Graph of percentage survival of 769-P RPMI against concentration of Drug X. Inhibition of growth was observed over a range of concentrations, spanning 20-100µM.

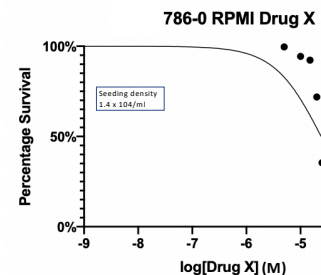


Figure 5b
Graph of percentage survival of 786-0 RPMI against concentration of Drug X. Inhibition of growth was observed over a range of concentrations, spanning 1-100µM.

Drug Combination Results

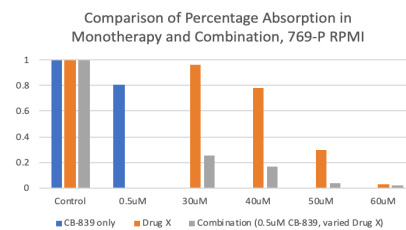


Figure 6a
Graph showing relationship between drug concentration (X axis) absorption of light (Y axis) in 769-P RPMI.

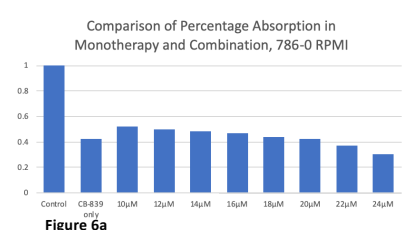


Figure 6a
Graph showing relationship between drug concentration in combination (X axis) with light absorption (Y axis) in 786-0 RPMI. 0.5µM CB-839 was present in each well (except for control) with concentration of Drug X varied as shown above.

Discussion

As outlined above, the primary objective of this vacation scholarship is to investigate our hypothesis, that CB-839 and Drug X show synergy when cells are treated with them simultaneously. While researching this idea, it became apparent that drug synergy is a very strictly defined concept that can only be proven by rigorous, complex statistical analysis, namely by calculating a CI index (see figure 7). ONLY if this analysis holds true and the definition of synergy is fulfilled will any results benefit patients. The analysis is performed by CalcuSyn software, though as a prerequisite each drug must have a sigmoidal dose response curve with strong R-values (6). The plateau effect seen with CB-839 (see figure 4b) complicated this, proving to be an obstacle to computational analysis. However, it is possible to comment, based on trends in the data, whether any relationship is present between CB-839 and Drug X in combination; I will do so below.

- Additive/synergistic effect suggested with CB-839 + Drug X in 769-P RPMI line.
- Cell lines in MEM appeared more sensitive to each drug, compared to RPMI.
- 786-0 cell line is the most sensitive to each drug; 769-P RPMI is the most resistant.

$$CI = \frac{IC_{50} \text{ of A in combination test}}{IC_{50} \text{ of A in single drug test}} + \frac{IC_{50} \text{ of B in combination test}}{IC_{50} \text{ of B in single drug test}}$$

Figure 7
Equation for calculating CI index, quantifying synergy. (7)

References

- <https://www.cancer.org/cancer/kidney-cancer/detection-diagnosis-staging/detection.html> (1)
- https://www.calithera.com/wp-content/uploads/2017/12/GTC-BIO_Nov-16-2015.pptx-Read-Only.pdf (3)
- <https://www.ncbi.nlm.nih.gov/pubmed/26354425> (5)
- <https://www.ncbi.nlm.nih.gov/pubmed/20068163> (6)
- <https://www.calithera.com/wp-content/uploads/2017/12/AACR-2015-final.pdf> (2)
- <https://www.calithera.com/pipeline/> (4)
- <https://pubs.rsc.org/en/content/articlelanding/2015/tb/c5tb00904a#divAbstract> (7)